ACS Photonics

pubs.acs.org/journal/apchd5

Article

Room Temperature Graphene Mid-Infrared Bolometer with a Broad Operational Wavelength Range

Shaofan Yuan,[⊥] Renwen Yu,[⊥] Chao Ma, Bingchen Deng, Qiushi Guo, Xiaolong Chen, Cheng Li, Chen Chen, Kenji Watanabe, Takashi Taniguchi, F. Javier García de Abajo,* and Fengnian Xia*

Cite This: *ACS Photonics* 2020, 7, 1206−1215

Read Online

ACCESS | Metrics & More | Article Recommendations | Supporting Information

ABSTRACT: The past decade has witnessed the realization of numerous different types of graphene photodetectors with a strong focus on the visible and near-infrared spectral range, in which various high-performance photodetectors exist based on traditional materials such as silicon and III−V compound semiconductors. However, high-speed mid-infrared photodetection at room temperature is still an unsolved challenge, despite its importance in applications such as security, sensing, and imaging. Here we address this challenge by demonstrating that high-quality graphene is an ideal high-speed bolometric material for the less-explored yet critical mid-infrared photodetection at room temperature, due to its broadband absorption, small heat capacity, and remarkably large temperature coefficient of resistance (TCR) of up to around 1% per Kelvin, which is comparable to that of commercial bolometric materials. We demonstrate a device based on graphene encapsulated in hexagonal boron nitride (hBN) exhibiting decent extrinsic responsivities of 5.1−1.4 mA/W in the 3.4−12 μm wavelength range at room temperature, and further predict a detection bandwidth of at least 47 MHz. Our demonstration lays the foundations for graphene high-speed mid-infrared technologies.

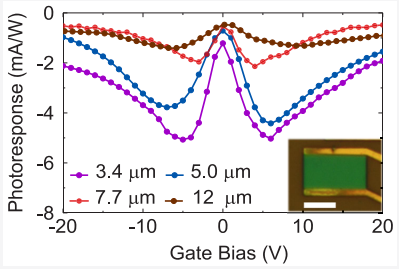

KEYWORDS: *mid-infrared bolometer, broad wavelength range, high-quality graphene, scattering channels, temperature coefficient of resistance*

The mid-infrared wavelength regime (~2−14 μm) is routinely exploited for many important applications in biomedical sensing,[1,2] thermal imaging,[3] and free-space optical communications.[4] For example, based on the distinctive vibrational resonances that most molecules exhibit in this mid-infrared wavelength range, infrared spectroscopy has been widely used to identify chemicals and biomolecules.[1] Additionally, the 3−5 μm and 8−13 μm ranges are two important atmospheric transmission windows, in which absorption by air molecules is minimal.[5] Furthermore, Rayleigh scattering at these long wavelengths is much weaker than that in the visible and near-infrared regions because the scattering intensity is inversely proportional to the fourth power of the wavelength.[6] As a result, these spectral ranges may also be ideal for future free-space communications and light detection and ranging (LIDAR) applications for autonomous driving.[4,7] However, conventional highly sensitive mid-infrared photodetectors leveraging interband absorption are made from narrow gap materials, such as mercury cadmium telluride (MCT).[8] They usually require liquid nitrogen cooling, making their large-scale deployment challenging.[8] In contrast, microbolometers are primarily used for room-temperature mid-infrared photodetection and imaging,[3] but they generally have a low operational speed, typically below a few kilohertz, due to their large heat capacitance and high thermal insulation.[3] Additionally, the thermal insulation required by bolometers involves a complete suspension of the detection elements,[3] which renders the fabrication of microbolometer array imagers challenging.[3] Consequently, new types of mid-infrared photodetectors and imagers with high sensitivity and operational speed at room temperature are in demand. Although graphene has previously been exploited for mid-infrared photodetection applications, intentionally leveraging induced trap states for high responsivity,[9,10] the demonstrated devices were usually very slow (in the Hz range) because of the long photocarrier trapping time by the defects. Moreover, graphene mid-infrared plasmonic photodetectors usually have narrow operational wavelength ranges due to the good quality factors of their plasmonic resonances.[11,12] Interestingly, new techniques have become available to overcome these wavelength limits by leveraging optical structures, such as gold-patched graphene nanostripes[13] and tubular three-dimensional nanomembranes.[14,15] These structures can have multiple resonance wavelengths and thus show improved photoresponsivities over a broader spectral range. Stacking layered metallic materials or

Received: January 7, 2020
Published: March 30, 2020

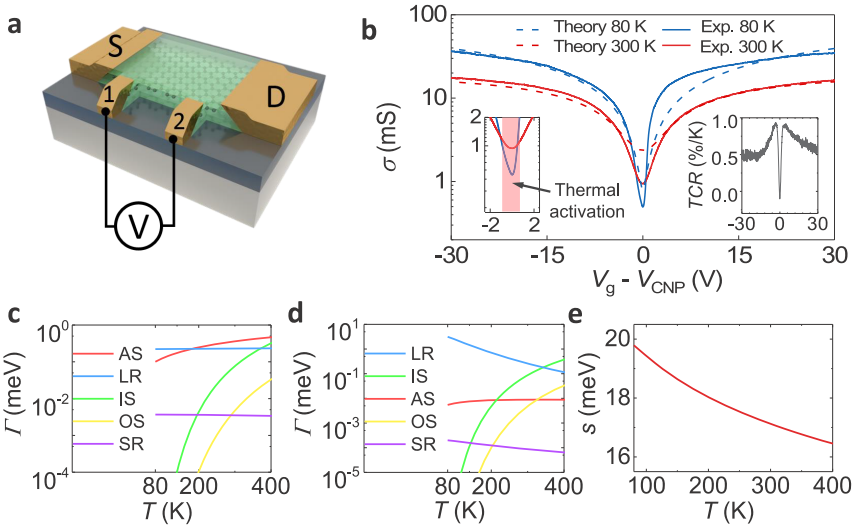

Figure 1. hBN-encapsulated graphene device configuration, transport characterization, and transport modeling. (a) Schematic of hBN-encapsulated graphene device based on a four-probe configuration, showing the source (S), drain (D), and voltage (V) applied between contacts 1 and 2. (b) Measured (solid curves) and calculated (dashed curves) conductivity σ of hBN-encapsulated graphene as a function of gate voltage V_g at 80 K (blue) and 300 K (red). Left inset: zoomed-in view of the conductivity around the charge neutrality point (CNP). Right inset: temperature coefficient of resistance (TCR = $(\Delta R/\Delta T)/R_0(T)$) as a function of gate voltage V_g at 300 K, where ΔR and ΔT are the change in resistivity and temperature in the four-probe measurements, respectively, and $R_0(T)$ is the resistivity at temperature T. (c) Partial contributions to the scattering strength Γ produced by all channels, including acoustic phonons (AS), long-range impurities (LR), intervalley scattering (IS), optical phonons (OS), and short-range impurity scattering (SR), as a function of temperature at Fermi energy $E_F = -160$ meV in the metallic regime. (d) Same as (c) at the CNP. (e) Strength of potential fluctuations s as a function of temperature at the CNP.

semiconductors to form heterojunctions also provides a new pathway to design high-performance broadband mid-infrared photodetectors.[16−19] Besides the mid-infrared, there have also been several demonstrations of layered materials for photodetection in the terahertz[20−22] and in the visible and near-infrared[23−28] spectral ranges.

Here, we demonstrate a fast broadband room-temperature mid-infrared bolometer based on high quality graphene encapsulated in hexagonal boron nitride (hBN). We thoroughly investigate the photocurrent generation mechanisms at different doping levels in the heterostructure, which turn out to be distinctively different from all previous demonstrations[23,29−32] due to the substantial enhancement of the graphene quality. Specifically, the temperature-sensitive transport properties enable a high responsivity, which, combined with the gapless band structure and exceptionally low heat capacity of graphene, renders broadband and high-speed photodetection in the mid-infrared range possible.[33]

RESULTS AND DISCUSSION

Figure 1a is the schematic of a typical hBN-encapsulated graphene device used in this work. The graphene is sandwiched by hBN flakes and transferred onto a silicon substrate covered with a 90 nm layer of silicon dioxide. We first characterize the graphene transport properties based on a four-probe measurement scheme.[34] The heterostructure is shaped into four-terminal geometry using plasma etching, and then chromium/gold (5/45 nm) is deposited to make edge contact with the graphene.[35] The hBN encapsulation minimizes contamination of the device during fabrication and preserves the high graphene quality.[34,35] The conductivity, $\sigma = \frac{I_{ds}}{V_1 - V_2} \cdot \frac{W}{L_{1,2}}$, is measured in a four-probe configuration, where $W = 1.4$ μm is the channel width, $L_{1,2} = 2$ μm is the length between probes 1 and 2, I_{ds} is the source-drain (S−D) current, and V_1 and V_2 are voltages collected by probes 1 and 2, respectively (see Figure 1a). We plot the graphene conductivity as a function of gate bias (V_g) at 80 and 300 K in Figure 1b. The inset is an enlarged view around the charge neutrality point (CNP, corresponding to a gate voltage V_{CNP}). In this measurement scheme, the carrier density n in graphene is determined by the capacitor equation $n = C_g(V_g - V_{CNP})/e$, where $C_g = \left(\frac{d_{SiO2}}{\varepsilon_0 \varepsilon_{SiO2}} + \frac{d_{hBN}}{\varepsilon_0 \varepsilon_{hBN}}\right)^{-1} = 1.03 \times 10^{-4}$ F/m^2 is the gate capacitance per unit area, e is the elementary charge, $\varepsilon_{SiO2/hBN}$ is the relative DC permittivity of SiO_2/hBN, and d_{SiO2} = 90 nm (d_{hBN} = 35 nm) is the thickness of the SiO_2 (hBN) layer. Furthermore, the Fermi energy scales with carrier density n as $E_F = \hbar v_F \sqrt{\pi n}$, where $\hbar$ is the Planck constant, $v_F = 10^6$ m/s is the Fermi velocity.[36] As shown in Figure 1b, the charge carrier density in graphene can be continuously tuned by varying V_g to drive the device into two different regimes: a thermal activation regime around the CNP and a metallic regime at higher carrier densities.[33,37] When the gate bias relative to V_{CNP} is less than ~0.7 V ($|V_g - V_{CNP}| < 0.7$ V), we observe an insulating behavior against temperature T (i.e., $d\sigma/dT > 0$), which can be attributed to the influence of electron−hole puddles close to the CNP.[34,38] In contrast, when the gate bias exceeds 0.7 V ($|V_g - V_{CNP}| > 0.7$ V; graphene is sufficiently doped), we observe a metallic behavior characterized by $d\sigma/dT < 0$. At 300 K, our calculations of the temperature coefficient of resistance (TCR = $(\Delta R/\Delta T)/R_0(T)$) yield 0.54% K^{-1} and 0.95% K^{-1} for $E_F = -160$ meV and −56 meV, respectively (see right inset of Figure 1b), where ΔR and ΔT are the changes in resistivity and temperature in the four-probe measurements, and $R_0(T)$ is the resistivity at temperature T. The related transport data are shown in Supporting Information Section 1. Our theoretical model (dashed curves in Figure 1b) captures the major

https://dx.doi.org/10.1021/acsphotonics.0c00028
ACS Photonics 2020, 7, 1206−1215

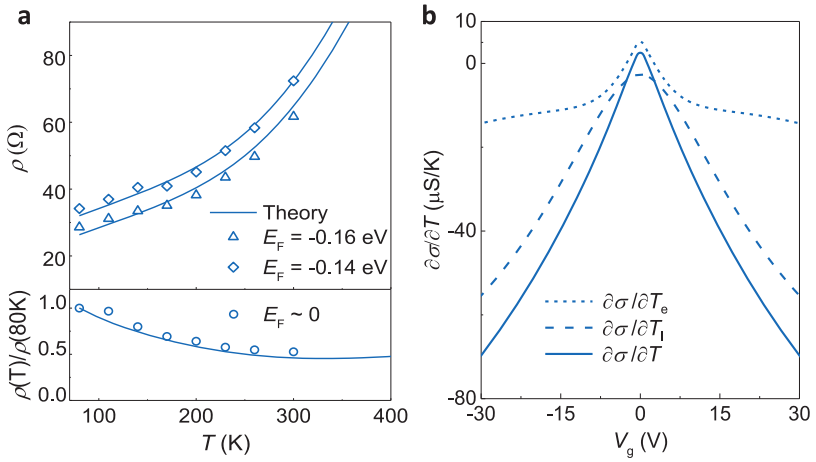

Figure 2. Temperature-dependence of carrier transport properties in hBN-encapsulated graphene. (a) Top: measured resistivity as a function of temperature at $E_F = -140$ meV (diamonds) and -160 meV (triangles), compared with theoretical calculations (solid curves). The sample mobility is 54 000 cm^2/(V·s) at $E_F = -160$ meV (hole density $n = +1.8 \times 10^{12}$ cm^{-2}). Bottom: resistivity ratio $\rho(T)/\rho(80\text{K})$ as a function of temperature T at the CNP in experiments (circles) and theory (solid curve). (b) Derivatives of the conductivity with respect to electron temperature (T_e, short dashed curve), phonon temperature (T_l, long dashed curve), and equilibrium-state sample temperature (T, solid curve).

features of both the gate and the temperature dependence. In particular, our theory reproduces the metallic-insulating-transition behavior (see Figure 1b). In order to capture the main transport properties over a broad range of doping levels, we model the metal-like diffusive transport at high doping taking intervalley phonon scattering (IS), acoustic phonon scattering (AS), low-momentum optical phonon scattering (OS), short-range impurity scattering (SR), and long-range impurity scattering (LR) into account.[39−42] To simulate the transport properties close to the CNP, we also consider the distribution of fluctuating local potentials,[43] which leads to an activated transport behavior. More details about the theoretical framework are given in Section 2 of the Supporting Information, while the contribution of different channels to the scattering strength Γ is presented in Figure 1c and 1d for metallic and thermal activation regimes, respectively. Theoretical simulations are performed in accordance with the experimental hole transport conditions (see Supporting Information Section 2 for details); in fact, due to electron−hole asymmetry,[38,44] the transport is sensitive to the sign of the charge carriers. Since LR impurities are usually charged, their scattering strength can be strongly affected by the electrostatic screening of graphene. Because electrostatic screening is particularly sensitive to temperature around the CNP, one finds a stronger temperature dependence in LR scattering strength around the CNP when comparing Figure 1c and 1d (see Supporting Information Section 2 for more details).

As shown in Figure 1c ($E_F = -160$ meV), intervalley phonon scattering (IS) and acoustic phonon scattering (AS) are the two dominant contributions to electron−phonon scattering in the metallic regime. Electrons are scattered between K and K′ valleys of the Brillouin zone by high-momentum optical phonons in IS, whereas AS only leads to minor changes in both momentum and energy. The scattering between electrons and low-momentum optical phonons (OS) is negligibly weak because the small Fermi surface in graphene imposes a strong kinematical constraint on low-momentum scattering.[45,46] Besides intrinsic phonon scatterings, long- and short-range impurity scattering (LR and SR in Figure 1c) can also play an important role, though the density of impurities has been reduced by the use of a dry transfer technique in our samples.[34,35] In fact, as shown in Figure 1c, LR scattering dominates when the temperature is below ∼180 K. In contrast to impurity scattering channels, all phonon scattering channels are sensitive to temperature variations and their scattering strengths increase with temperature. This indicates that $d\sigma/dT$ is dominated by phonon scatterings at this doping level, which leads to metallic behavior ($d\sigma/dT < 0$). Consequently, reducing the density of impurities and improving sample quality can make transport more sensitive to temperature because phonon scattering plays a more important role. This therefore improves the performance of graphene bolometers operating in the metallic regime.

In contrast to the metallic regime, the thermal activation regime around the CNP is regulated by the coexistence of activated transport and regular diffusive transport.[38,43] Thermal activation facilitates carrier transport through the potential landscape due to the presence of electron−hole puddles.[47] Moreover, long-range impurities provide a major scattering channel around the CNP in diffusive transport, especially at low temperatures (see Figure 1d) because of the weak static screening.[48] Although the calculated conductivity at the Dirac point (see Figure 1b) does not match well the experimental results, we emphasize that this quantitative discrepancy between theory and experiment at the CNP has been reported in numerous previous publications.[49−51] In our case, we attribute the discrepancy to the difficulty in extracting charged impurity densities accurately based on the measurement of the conductivity in the metallic regime[49] (see Supporting Information Section 2). However, our calculated results capture well the temperature dependence and the properties of the metallic-insulating-behavior transition. Notably, when moving from a Fermi level $E_F = -160$ meV (Figure 1c) to $E_F \approx 0$ (Figure 1d), long-range impurity scattering becomes dominant over other scattering channels due to the reduction in the strength of screening, and also electron−phonon scattering becomes weaker. However, close to the CNP (Figure 1d), the strength of long-range impurity scattering decreases when the temperature increases due to stronger screening;[38,48] this is in stark contrast to the behavior of electron−phonon scattering. Besides the regular diffusive transport at the CNP, the coexistent activated transport can

https://dx.doi.org/10.1021/acsphotonics.0c00028
ACS Photonics 2020, 7, 1206−1215

be characterized by an activated conductivity determined by s (plotted in Figure 1e), which represents the strength of potential fluctuations. The long-range impurity scattering and potential fluctuations at the CNP together produce an insulating behavior ($d\sigma/dT > 0$). Details on these calculations are presented in Supporting Information Section 2.

In some of the previously reported graphene devices, carrier transport was found to display a weak temperature dependence across a wide temperature range because scattering by impurities, defects, and grain boundaries dominated the transport and these extrinsic scattering channels tended to be temperature insensitive.[12,38] Previous efforts of patterning graphene into nanostructures resulted in moderate TCR,[12,52,53] while at the same time enhancing electron−phonon coupling and the related energy dissipation via disorder-assisted supercollision cooling.[46] In contrast, here we show that TCR is greatly enhanced in high-quality graphene because of significantly reduced impurity scattering. The quality of graphene samples can be evaluated by examining the carrier mobility, which is strongly affected by the density of charged impurities.[34] We estimate the carrier mobility in graphene using $\mu = 1/(ne\rho)$,[54] where ρ is the resistivity. The sample under consideration shows a carrier mobility of 54 000 $cm^2/(V{\cdot}s)$ at $E_F = -160$ meV ($n = +1.8 \times 10^{12}$ cm^{-2}). To understand its behavior, we simulate the temperature dependence of the resistivity for both metallic and thermal activation regimes (see details in Supporting Information Section 2) using a model that captures well the temperature dependence of carrier transport at two different Fermi levels ($E_F = -140$ and -160 meV), as shown in the top panel of Figure 2a. At the CNP, the resistivity measurements display larger fluctuations than those in the metallic regime. Moreover, there is a mismatch between experiment and theory on the absolute value of the minimum conductivity, similar to numerous previous reports, which we attribute to the uncertainty introduced by electron−hole puddles close to the CNP.[49−51] To reconcile this discrepancy, in the bottom panel of Figure 2a, we plot the resistance at the CNP normalized to that measured at 80 K. One can also see that the resistivity decreases slowly with temperature at 300 K at the CNP, while in the metallic regime the resistivity increases at higher temperature due to stronger electron−phonon scattering (see Figure 1c);[38,47] in contrast, a decrease in resistivity is expected at the CNP, where thermal activation transport dominates. Remarkably, carrier transport is temperature sensitive in our samples due to the largely reduced impurity scattering. The TCR reaches 0.95% K^{-1} at $E_F = -56$ meV, which is only about twice smaller than the TCR of VO_x films in commercial bolometers (TCR ∼ 2% K^{-1}).[55]

On the basis of our transport model, we further calculate the impact of the variation of electron temperature (ΔT_e) and phonon temperature (ΔT_l) on the electrical conductivity. Assuming an initial temperature T_s at equilibrium without external illumination, the generated photocurrent I_{ph} in a bolometer of channel width W and length L is determined by ΔT_e and ΔT_l as

$$I_{ph} \approx \frac{W}{L}\left(\left.\frac{\partial\sigma}{\partial T_e}\right|_{T_e=T_s,T_l=T_s}\Delta T_e + \left.\frac{\partial\sigma}{\partial T_l}\right|_{T_e=T_s,T_l=T_s}\Delta T_l\right)V_{ds} \quad (1)$$

where $\partial\sigma/\partial T_e$ and $\partial\sigma/\partial T_l$ are the rates of conductivity variation against changes in electron and phonon temperatures, respectively, and V_{ds} is the drain-source bias. Note that eq 1 also holds even when the electron and lattice temperatures are different ($T_e \neq T_l$), as it is the case when there is considerable Joule heating at a large V_{ds}. In order to show the general behavior of $\partial\sigma/\partial T_e$ and $\partial\sigma/\partial T_l$, we assume thermal equilibrium in our transport measurements ($T_e \approx T_l \approx 300$ K at $V_{ds} = 10$ mV), and then calculate and plot those derivatives in Figure 2b based on the scattering channels shown in Figure 1c,d (see Supporting Information Section 2 for more information). We observe that $\partial\sigma/\partial T_l$ remains negative regardless of the gate bias because the increase in lattice temperature T_l always reduces the mobility and conductivity. However, at low doping levels, the weaker electron−phonon coupling strength leads to a reduction in the magnitude of $\partial\sigma/\partial T_l$ (see Figure 2b). In contrast, $\partial\sigma/\partial T_e$ displays a nontrivial behavior as a function of the doping level due to the interplay between electron-impurity and electron−phonon scattering channels. This quantity switches sign around the CNP as a result of the onset of the activated transport together with the negative correlation between the electron-impurity scattering rate and the electron temperature close to the CNP (see LR curve in Figure 1d). In Figure 2b, we also plot the overall $\partial\sigma/\partial T$ derivative (solid curve) as a sum of $\partial\sigma/\partial T_e$ and $\partial\sigma/\partial T_l$. Considering different features of $\partial\sigma/\partial T_e$ and $\partial\sigma/\partial T_l$, heating electrons and phonons in the metallic regime is a more effective way to operate the graphene bolometer because both $\partial\sigma/\partial T_e$ and $\partial\sigma/\partial T_l$ are then negative.

After understanding carrier transport properties and their temperature dependence in hBN-encapsulated graphene, we fabricate a two-terminal device with dimensions of 6 × 10.5 μm^2 for photocurrent measurements (see optical image in the left inset of Figure 3). Here we do not use the four-terminal devices shown in Figure 1 for photodetection because the graphene edges and corners in such high mobility devices can significantly affect the photocurrent generation.[56] This photocurrent could stem from collinear electron−electron scattering in charge-neutral graphene.[48] Recently the photothermo-

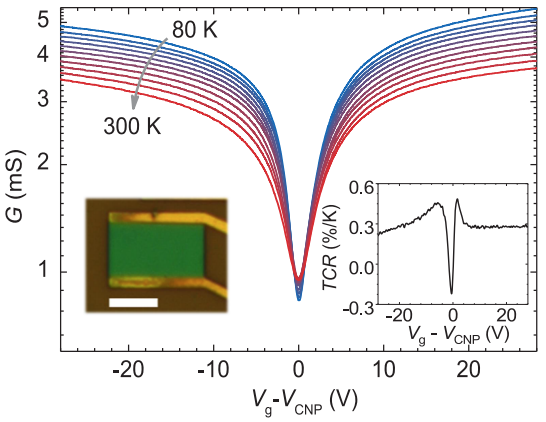

Figure 3. Transport properties of a two-terminal hBN-encapsulated graphene bolometric device. Sheet conductance as a function of gate voltage V_g at different temperatures from 300 K (red curve) to 80 K (blue curve). The left inset shows an optical image of the measured two-terminal device. Scale bar: 5 μm. The right inset shows the experimentally determined temperature coefficient of resistance (TCR) as a function of gate voltage V_g at 300 K, calculated as $TCR = (\Delta R/\Delta T)/R_0$, where $\Delta R = R_1 - R_2$, R_1 and R_2 are the resistances measured at 300 and 290 K, respectively, $\Delta T = 10$ K, and $R_0 = (R_1 + R_2)/2$.

https://dx.doi.org/10.1021/acsphotonics.0c00028
ACS Photonics 2020, 7, 1206−1215

electric effect induced by the fringing fields around the edges and corners has also been invoked to explain this phenomenon.[57] Figure 3 shows the conductance $G = I_{ds}/V_{ds}$ as a function of gate voltage V_g, where I_{ds} and V_{ds} are the source-drain current and voltage, respectively. The transfer curves measured using the two-terminal configuration show similar metallic-insulating-behavior transition as shown in Figure 1b. The right inset shows the TCR as a function of gate voltage at 300 K. Even though contact resistance is included in the two-terminal measurement, the TCR is as high as ∼0.5% K^{-1} for $E_F = -73$ meV at room temperature. From our measurements in multiple four-terminal graphene devices, we estimate that the edge contact resistivity lies in the 500−1000 Ω·μm range and is independent of temperature[35] when the Fermi-level is away from the CNP ($E_F < -140$ meV) (see Supporting Information Section 3 for more information). If we exclude a contact resistivity of 1000 Ω·μm from this two-terminal device, we estimate that the carrier mobility is 22 000 $cm^2/(V{\cdot}s)$ when $E_F = -160$ meV. The variability in the device fabrication, especially for edge-contacted devices, may cause different two-terminal mobilities. Although this mobility is smaller than that of the four-terminal device presented previously, the main features of the transport properties are similar, such as the metallic-insulating-behavior transition near the CNP and the remarkable TCR.

We characterize the photoresponse of this two-terminal device at light excitation wavelegnths of 3.4, 5.0, 7.7, and 12 μm, respectively, at a fixed source-drain bias $V_{ds} = 0.5$ V. The infrared light is mechanically chopped at frequency f_m and focused on the device, and the generated photocurrent (I_{ph}) is amplified by a preamplifier and collected by a lock-in amplifier with reference to f_m. The measured extrinsic responsivity, $R_{ex} = I_{ph}/P_{dev}$, where P_{dev} is the incident power on the graphene device (see Methods), is plotted in Figure 4a as a function of gate bias for the four wavelengths at $f_m = 980$ Hz. Details of the photocurrent measurement and responsivity calibration can be found in Supporting Information Section 4. Our device exhibits strong photoresponse at all four excitation wavelengths due to the gapless nature of graphene.[33] The peak responsivities of this graphene bolometer are observed around $|V_g - V_{CNP}| = 6$ V for excitation wavelengths of 3.4, 5.0, and 12 μm, approximately where the TCR is maximum (see inset of Figure 3). We suspect that the shift of the peak position at 7.7 μm is due to the impact of hBN hyperbolic phonons on the graphene light absorption,[58] although further investigation is needed to clarify the exact causes. The maximum measured responsivities (5.1, 4.4, 2.1, and 1.4 mA/W at 3.4, 5.0, 7.7, and 12 μm, respectively, with $V_{ds} = 0.5$ V) are around 1 order of magnitude larger than in previous works (0.25 mA/W at λ = 690 nm and $V_{ds} = 1$ V),[31] although the responsivity in this study is measured at much longer wavelengths and smaller V_{ds}. We expect that the responsivity will be much smaller than 0.25 mA/W for graphene on silicon oxide in the mid-infrared,[31] because electron and hole puddles are abundant in such configuration and these puddles should further reduce the absorption of low-energy photons.[36,59] This significant improvement is mainly due to the high-quality graphene used here, in which the carrier transport properties are very sensitive to temperature. At 80 K, the responsivities are improved significantly and show similar line shapes as those measured at 300 K (see Supporting Information Section 5). To our knowledge, this ultrabroadband, giant intrinsic photoresponse has not been previously reported in graphene at mid-infrared wavelengths without any artificial photonic structures. We expect that coupling graphene to previously demonstrated photonic structures can improve the device performance further by more than one order of magnitude.[13,14] Moreover, the photoresponse reported in Figure 4a is negative, indicating an increase in carrier scattering and a reduction in conductivity under light excitation regardless of the gate bias, a typical bolometric effect in metals. To experimentally rule out other mechanisms reported in previous asymmetric and patterned devices,[56,60] such as thermoelectric and intrinsic edge photocurrent generation, we perform a spatial photocurrent mapping of our device at 1.3 μm wavelength (see Supporting Information Section 6). The negative photocurrent in the entire device confirms the bolometric mechanism since both thermoelectric and edge photocurrent would result in two opposite polarities in the photocurrent mapping.[56,60]

Besides these remarkably large negative peak responsivities, the response is strongly dependent on the gate bias V_g and shows two important features (see Figure 4a): first, the amplitude of R_{ex} decreases when we further increase the gate bias amplitude $|V_g - V_{CNP}|$ above ∼6 V; second, R_{ex} drops significantly around the CNP. Although most previous graphene photodetectors also show a gate bias dependence,[13,31] the results presented in Figure 4a are distinctively different. The responses from two additional devices can be found in Supporting Information Section 7, where we also discuss the relationship between mobility and photoresponse. To explain these features in more detail, we further simulate the elevations of the electron and phonon temperatures, from which we calculate the photoresponse based on the temperature dependence of the conductivity. In Figure 4b, we plot the calculated responsivity and electron/lattice temperature variation upon excitation with 5 μm light. We use a two-temperature model to self-consistently calculate the temperature elevations $\Delta T_{e/l}$ under light irradiation. We note that calculated results (Figure 4b) are based on the extracted

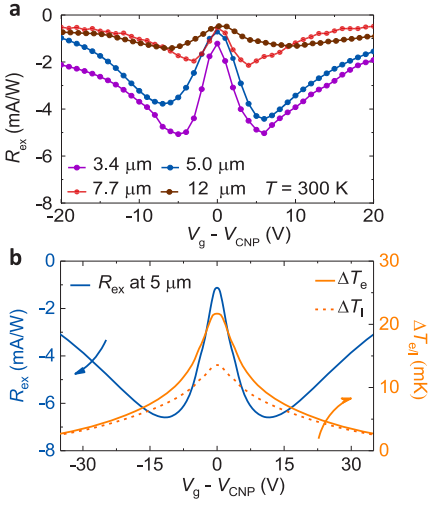

Figure 4. Broadband mid-infrared photoresponse in hBN-encapsulated graphene at room temperature. (a) Room temperature extrinsic responsivity as a function of gate bias voltage under laser excitation at 3.4, 5.0, 7.7, and 12 μm light wavelengths (see labels). The source-drain bias is $V_{ds} = 0.5$ V. (b) Calculated extrinsic responsivity at 5.0 μm (blue curve, left vertical axis) and increase in electron temperature ΔT_e (orange solid curve, right vertical axis) and lattice temperature ΔT_l (orange dashed curve, right vertical axis).

https://dx.doi.org/10.1021/acsphotonics.0c00028
ACS Photonics 2020, 7, 1206−1215

parameters of our four-terminal device, taken from Figures 1 and 2a; our four-probe measurements allow us to extract scattering parameters accurately. As a result, the theoretical results in Figure 4b are only intended to capture the main gate-dependent features in Figure 4a, and the observed differences in detailed performance metrics with those in Figure 4a are expected. In the two-temperature model, we calculate the electron−phonon cooling power considering all of the aforementioned three types of phonon modes[41] (see Supporting Information Section 8 for details of our model). Then, the photocurrent can be computed as $(W/L)[\sigma(T_1 + \Delta T_e, T_2 + \Delta T_l) - \sigma(T_1, T_2)]V_{ds}$, where T_1 and T_2 are the electron and lattice temperatures in the absence of illumination, while ΔT_e and ΔT_l are the temperature elevations of electrons and phonons under light excitation, respectively. Compared with the measured responsivity (Figure 4a), our theoretical results capture the main features of the R_{ex} dependence on V_g at 5 μm wavelength (blue curve in Figure 4b). We observe that the extrinsic responsivity gradually decreases when $|V_g - V_{CNP}| > 6$ V in experiment. This phenomenon can be attributed to two reasons. First, when the graphene is highly doped ($|E_F| > E_{ph}/2$, where E_{ph} is the incident photon energy), absorption of infrared photons due to interband transitions is suppressed due to Pauli blocking[61] (see calculated absorption at 5.0 μm as a function of V_g in Section 9 of the Supporting Information). Moreover, the wider Fermi surface at high doping also increases the available phase space for inelastic electron collisions, and thus, the electron−phonon scattering strength is increased, which leads to more efficient heat dissipation.[45] These two factors produce a reduction of ΔT_e and ΔT_l at large doping levels. Our model also captures the second feature, a sharp drop in photoresponse around the CNP. As shown in Figure 2b, near the CNP, $\partial\sigma/\partial T_e$ and $\partial\sigma/\partial T_l$ are much smaller than those in the metallic regime. Moreover, ΔT_e and ΔT_l produce opposite effects on the photocurrent at the CNP ($\partial\sigma/\partial T_e > 0$ and $\partial\sigma/\partial T_l < 0$) and partly offset each other. Therefore, the significant reduction in photoresponse observed around the CNP is not surprising. At this point, we emphasize that our experimental conditions are still different from the equilibrium state at the CNP shown in Figure 2b, because we use a source-drain bias $V_{ds} = 0.5$ V in the photocurrent measurement. The involved temperatures $T_1 \sim 430$ K and $T_2 \sim 350$ K are notably higher than the ambient temperature because of the Joule heating effect. The resulting overall bolometric photoresponse given by

$$\left.\frac{\partial\sigma}{\partial T_e}\right|_{T_e=T_l, T_l=T_2} \Delta T_e + \left.\frac{\partial\sigma}{\partial T_l}\right|_{T_e=T_l, T_l=T_2} \Delta T_l$$

is still negative even at the CNP (see Supporting Information Section 8 for more details). We note that the magnitude of $\partial\sigma/\partial T_l$ is enhanced in our high-quality sample compared to graphene on silica[31] and dominates the photoresponse of our device. This enhanced $\partial\sigma/\partial T_l$ explains the absence of the photoconduction peak observed in ref 31 and also accounts for the much improved extrinsic responsivity in our device.

Finally, we evaluate the frequency response of our graphene devices. The heat capacity of graphene is orders of magnitude smaller than that of traditional bolometers, in which light absorbing and resistance layers are made from different materials of submicron thickness.[3] This small heat capacity of graphene enables high-bandwidth bolometer applications, while the operational speed of conventional bolometers is usually well below one kilohertz.[3] The performance of our device does not show any noticeable degradation up to 10 kHz (the measurement frequency limit in our mechanical chopper), as shown in Figure 5 (right axis). Since the speed is largely

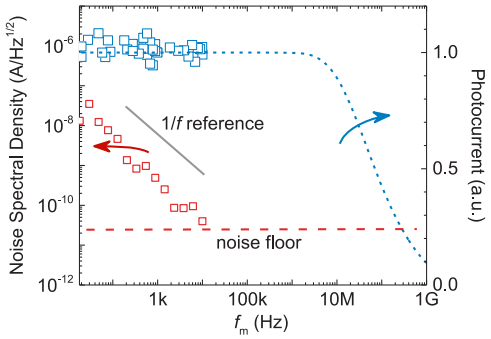

Figure 5. Frequency response and noise characteristics. We plot the noise current spectral density as a function of frequency at $V_{ds} = 0.5$ V and 300 K (left axis). The red dashed curve is the theoretical noise current spectral density associated with the combined effect of Johnson noise, thermal-fluctuation noise, and shot noise in our device. Experimental values (red squares) are close to our calculations at high frequencies f, where $1/f$ flicker noise is suppressed. The photoresponse is independent of modulation frequency f_m up to at least 10 kHz (right axis), which is the upper measurement limit of our setup. Theoretical calculations based on thermal dissipation analysis yield a 3 dB cutoff frequency of around 47 MHz in our device, as shown by the blue dashed curve.

determined by the thermal time constant, it should not be sensitive to the incidence wavelength. In Supporting Information Section 10, we show that the photoresponse is independent of f_m below 10 kHz at wavelengths of 5.0, 7.7, and 12 μm.

We further estimate the thermal response time τ of our graphene bolometer from the relation[3]

$$\tau = C_h/G_{th}$$

where C_h is the heat capacitance of the graphene absorber and G_{th} is its thermal conductance to heat sinks. Note that we estimate a heat capacitance $C_h = 2 \times 10^{-13}$ J/K including the effects of both electrons and phonons.[62] (see Supporting Information Section 10) The thermal conductance G_{th} between the electrons in graphene and the thermal sink is around 8.7×10^{-6} W/K at $|V_g - V_{CNP}| \approx 6$ V, where our device presents a maximum extrinsic responsivity. As a result, our estimated response time represents an upper limit of around 21 ns, corresponding to a 3-dB cutoff frequency of around 47 MHz, as shown by the solid blue curve in Figure 5. In fact, high-speed graphene photodetectors with operational speed well above 10 GHz have been reported by several groups including ours.[27,63,64] Although the photodetection mechanisms could be different in these previously reported graphene photodetectors, their similar RC time constant controls their electrical speed. The fact that those reported graphene photodetectors operate at gigahertz speed also indicates that the electrical time constant can be ignored, since here we report a much lower, conservatively estimated thermal speed of 47 MHz. More details regarding the frequency response of our bolometers can be found in Supporting Information Section 10. The high-speed operation of our device also circumvents the $1/f$ flicker noise at low frequencies,[65] which is orders of magnitude stronger than the combined effect of Johnson noise,

https://dx.doi.org/10.1021/acsphotonics.0c00028
ACS Photonics 2020, 7, 1206−1215

thermal-fluctuation noise, and shot noise.[66] We show the measured noise current spectral density below 10 kHz in Figure 5 (left axis). Indeed, we find that $1/f$ noise is suppressed significantly at higher frequencies: the noise current spectral density ($\sqrt{\langle \delta i^2 \rangle}$) follows a $1/f$ trend and is close to the theoretical white noise at 10 kHz (red dashed curve, 16 pA/Hz$^{1/2}$ for V_{ds} = 0.5 V at room temperature, see calculation details in Supporting Information Section 11), as shown in Figure 5. Since our device can operate at high frequencies ($f_m \gg 10$ kHz), we use the theoretical white noise to estimate the noise equivalent power (NEP) using the relation NEP = $\sqrt{\langle \delta i^2 \rangle}/R_{ex}$. We find a room-temperature NEP of 3, 3.6, 7.5, and 11 nW/Hz$^{1/2}$ at 3.4, 5.0, 7.7, and 12 μm illumination wavelength, respectively. Although the NEP reported here is large compared with the NEP of state-of-the-art microbolometers (~10 pW/Hz$^{1/2}$ at room temperature below 1 kHz),[3] the operational speed of the graphene bolometers is at least 5 orders of magnitude higher. In addition to microbolometers, narrow gap III–V materials such as Indium Antimonide (InSb) have also been used in room-temperature mid-infrared light detection. For example, a room-temperature NEP of 245 pW/Hz$^{1/2}$ at 4.6 μm has been reported in an InSb mid-IR photodetector,[67] and this NEP is about an order of magnitude smaller than the value obtained in our graphene bolometer in this work. However, there is plenty of room for improvement for our graphene bolometers. Currently, it only absorbs 1 to 2% of the incident mid-IR light. Integration of graphene in optical cavities, back reflection mirrors, or waveguides may lead to near-unity absorption.[68,69] Moreover, better thermal isolation of the structure may reduce heat dissipation and lead to further temperature and photoresponse increase.[3] These improvements should significantly improve the NEP and make it appealing in future mid-IR technologies. Moreover, compared with InSb photodetectors, our graphene bolometer has a much wider operational wavelength range. Here we demonstrate light detection up to 12 μm but the cutoff wavelength of InSb photodetectors is around 6 μm. A table comparing the performances of different mid-infrared detectors is provided in Supporting Information Section 12. Finally, we want to comment on the operational temperature of our graphene bolometers. In conventional semiconducting InSb photodetectors, the performance improves significantly at cryogenic temperature due to strong suppression of dark current.[70] In contrast, the dark current of the graphene bolometer remains rather independent of temperature due to its metallic nature, and reducing the temperature only moderately enhances its performance through the improvement in responsivity. As a result, the graphene bolometers demonstrated in this work are most suitable for room-temperature applications.

CONCLUSION

In summary, the hBN-encapsulated graphene bolometer demonstrated here shows a broad operational wavelength range (from 1.3 to 12 μm) and a theoretical detection speed of 47 MHz at room temperature. The scattering channels and photocurrent generation mechanisms at different doping levels in the device are thoroughly investigated to understand its photoresponse behavior. Phonon scattering channels (acoustic phonon scattering, intervalley scattering, and optical phonon scattering) in high-quality graphene contribute to its improved TCR (up to 1% per Kelvin), and this temperature-sensitive transport enables its high responsivity to mid-infrared radiation. Together with the gapless band structure and exceptionally low heat capacity, these factors make broadband and high-speed mid-infrared photodetection possible in high-quality graphene.

METHODS

Fabrication of hBN-Encapsulated Graphene Device. Graphene and hBN thin flakes were first mechanically exfoliated from bulk crystals onto 90 nm-silicon-dioxide-covered silicon substrates (SiO_2/Si substrate). We then assembled the hBN/graphene/hBN heterostructures on a new SiO_2/Si substrate using a van der Waals stacking method.[35] The heterostructures were annealed at 873 K in flowing hydrogen/argon environment for 6 h to remove polymer residues. After defining the shape of the channel using a Vistec 100 kV electron beam lithography system, the devices were patterned in an Oxford Plasmalab 100 reactive ion etching (RIE) system. Finally, chromium/gold electrodes (5/45 nm) were thermally evaporated to contact the graphene sheet.

ASSOCIATED CONTENT

Supporting Information

The Supporting Information is available free of charge at https://pubs.acs.org/doi/10.1021/acsphotonics.0c00028.

The measured graphene TCR based on four-probe method; Transport model of hBN-encapsulated graphene device; Extraction of the contact resistance using a four-probe configuration; Photoresponsivity and speed characterizations; Photocurrent measured at 80 and 300 K; Spatially resolved photocurrent scanning measurement at 1.3 μm; Performance variation among devices and the dependence of responsivity on carrier mobility; Photocurrent model in the hBN/graphene/hBN heterostructure; Infrared absorption in the hBN/graphene/hBN heterostructure; Thermal dissipation analysis in the hBN/graphene/hBN heterostructure and frequency dependence of the photoresponse; Noise current density measurement and calculation; Comparison of device performance in different mid-infrared photodetectors (PDF)

AUTHOR INFORMATION

Corresponding Authors

F. Javier García de Abajo − *ICFO-Institut de Ciencies Fotoniques, The Barcelona Institute of Science and Technology, 08860 Castelldefels, Barcelona, Spain; Institució Catalana de Recerca i Estudis Avançats (ICREA), 08010 Barcelona, Spain;* orcid.org/0000-0002-4970-4565; Email: javier.garciadeabajo@nanophotonics.es

Fengnian Xia − *Department of Electrical Engineering, Yale University, New Haven, Connecticut 06511, United States;* orcid.org/0000-0001-5176-368X; Email: fengnian.xia@yale.edu

Authors

Shaofan Yuan − *Department of Electrical Engineering, Yale University, New Haven, Connecticut 06511, United States*

Renwen Yu − *ICFO-Institut de Ciencies Fotoniques, The Barcelona Institute of Science and Technology, 08860 Castelldefels, Barcelona, Spain*

https://dx.doi.org/10.1021/acsphotonics.0c00028
ACS Photonics 2020, 7, 1206−1215

Chao Ma − *Department of Electrical Engineering, Yale University, New Haven, Connecticut 06511, United States;* orcid.org/0000-0002-2879-3239
Bingchen Deng − *Department of Electrical Engineering, Yale University, New Haven, Connecticut 06511, United States*
Qiushi Guo − *Department of Electrical Engineering, Yale University, New Haven, Connecticut 06511, United States*
Xiaolong Chen − *Department of Electrical Engineering, Yale University, New Haven, Connecticut 06511, United States*
Cheng Li − *Department of Electrical Engineering, Yale University, New Haven, Connecticut 06511, United States*
Chen Chen − *Department of Electrical Engineering, Yale University, New Haven, Connecticut 06511, United States*
Kenji Watanabe − *National Institute for Materials Science, Tsukuba 305-0044, Japan;* orcid.org/0000-0003-3701-8119
Takashi Taniguchi − *National Institute for Materials Science, Tsukuba 305-0044, Japan;* orcid.org/0000-0002-1467-3105

Complete contact information is available at: https://pubs.acs.org/10.1021/acsphotonics.0c00028

Author Contributions

[⊥]S.Y. and R.Y. contributed equally to this work.

Notes

The authors declare no competing financial interest.

■ ACKNOWLEDGMENTS

We acknowledge financial support from the National Science Foundation EFRI-NewLAW program (1741693). We also thank the Office of Naval Research Young Investigator Program for partial support in the experimental setup. R.Y. and F.J.G.A. acknowledge support from the Spanish MINECO (MAT2017-88492-R and SEV2015-0522), the ERC (Advanced Grant 789104-eNANO), the Catalan CERCA Program, and Fundació Privada Cellex. K.W. and T.T. acknowledge support from the Elemental Strategy Initiative conducted by the MEXT, Japan and the CREST (JPMJCR15F3), JST. We thank Adi Levi and Prof. Doron Naveh at Bar-Ilan University for assistance on photocurrent measurements.

■ REFERENCES

(1) Griffiths, P. R. Fourier-Transform Infrared Spectrometry. *Science* **1983**, *222*, 297−302.
(2) Griffiths, P. R. Recent Applications of Fourier-Transform Infrared Spectrometry in Chemical and Environmental Analysis. *Appl. Spectrosc.* **1977**, *31*, 497−505.
(3) Kruse, P. W. *Uncooled Thermal Imaging Arrays, Systems and Applications*; SPIE Optical Engineering Press: Bellingham, 2001.
(4) Hao, Q.; Zhu, G. S.; Yang, S.; Yang, K. W.; Duan, T.; Xie, X. P.; Huang, K.; Zeng, H. P. Mid-Infrared Transmitter and Receiver Modules for Free-Space Optical Communication. *Appl. Opt.* **2017**, *56*, 2260−2264.
(5) Green, A. E. S.; Griggs, M. Infrared Transmission through the Atmosphere. *Appl. Opt.* **1963**, *2*, 561−570.
(6) Cox, A. J.; DeWeerd, A. J.; Linden, J. An Experiment to Measure Mie and Rayleigh Total Scattering Cross Sections. *Am. J. Phys.* **2002**, *70*, 620−625.
(7) Medina, A.; Gaya, F.; del Pozo, F. Compact Laser Radar and Three-Dimensional Camera. *J. Opt. Soc. Am. A* **2006**, *23*, 800−805.
(8) Rogalski, A. Hgcdte Infrared Detector Material: History, Status and Outlook. *Rep. Prog. Phys.* **2005**, *68*, 2267−2336.
(9) Zhang, Y. Z.; Liu, T.; Meng, B.; Li, X. H.; Liang, G. Z.; Hu, X. N.; Wang, Q. J. Broadband High Photoresponse from Pure Monolayer Graphene Photodetector. *Nat. Commun.* **2013**, *4*, 1811.
(10) Yu, X. C.; Dong, Z. G.; Liu, Y. P.; Liu, T.; Tao, J.; Zeng, Y. Q.; Yang, J. K. W.; Wang, Q. J. A High Performance, Visible to Mid-Infrared Photodetector Based on Graphene Nanoribbons Passivated with Hfo2. *Nanoscale* **2016**, *8*, 327−332.
(11) Yao, Y.; Shankar, R.; Rauter, P.; Song, Y.; Kong, J.; Loncar, M.; Capasso, F. High-Responsivity Mid-Infrared Graphene Detectors with Antenna-Enhanced Photocarrier Generation and Collection. *Nano Lett.* **2014**, *14*, 3749−3754.
(12) Guo, Q.; Yu, R.; Li, C.; Yuan, S.; Deng, B.; Garcia de Abajo, F. J.; Xia, F. Efficient Electrical Detection of Mid-Infrared Graphene Plasmons at Room Temperature. *Nat. Mater.* **2018**, *17*, 986−992.
(13) Cakmakyapan, S.; Lu, P. K.; Navabi, A.; Jarrahi, M. Gold-Patched Graphene Nano-Stripes for High-Responsivity and Ultrafast Photodetection from the Visible to Infrared Regime. *Light: Sci. Appl.* **2018**, *7*, 20.
(14) Deng, T.; Zhang, Z. H.; Liu, Y. X.; Wang, Y. X.; Su, F.; Li, S. S.; Zhang, Y.; Li, H.; Chen, H. J.; Zhao, Z. R.; et al. Three-Dimensional Graphene Field-Effect Transistors as High-Performance Photodetectors. *Nano Lett.* **2019**, *19*, 1494−1503.
(15) Wang, H.; Zhen, H. L.; Li, S. L.; Jing, Y. L.; Huang, G. S.; Mei, Y. F.; Lu, W. Self-Rolling and Light-Trapping in Flexible Quantum Well-Embedded Nanomembranes for Wide-Angle Infrared Photodetectors. *Sci. Adv.* **2016**, *2*, No. e1600027.
(16) Long, M. S.; Wang, Y.; Wang, P.; Zhou, X. H.; Xia, H.; Luo, C.; Huang, S. Y.; Zhang, G. W.; Yan, H. G.; Fan, Z. Y.; et al. Palladium Diselenide Long-Wavelength Infrared Photodetector with High Sensitivity and Stability. *ACS Nano* **2019**, *13*, 2511−2519.
(17) Wu, D.; Wang, Y. E.; Zeng, L. H.; Jia, C.; Wu, E. P.; Xu, T. T.; Shi, Z. F.; Tian, Y. T.; Li, X. J.; Tsang, Y. H. Design of 2d Layered PtSe2 Heterojunction for the High-Performance, Room-Temperature, Broadband, Infrared Photodetector. *ACS Photonics* **2018**, *5*, 3820−3827.
(18) Wu, E. P.; Wu, D.; Jia, C.; Wang, Y. G.; Yuan, H. Y.; Zeng, L. H.; Xu, T. T.; Shi, Z. F.; Tian, Y. T.; Li, X. J. In Situ Fabrication of 2d Ws2/Si Type-II Heterojunction for Self-Powered Broadband Photodetector with Response up to Mid-Infrared. *ACS Photonics* **2019**, *6*, 565−572.
(19) Wu, D.; Guo, J. W.; Du, J.; Xia, C. X.; Zeng, L. H.; Tian, Y. Z.; Shi, Z. F.; Tian, Y. T.; Li, X. J.; Tsang, Y. H.; et al. Highly Polarization-Sensitive, Broadband, Self-Powered Photodetector Based on Graphene/Pdse2/Germanium Heterojunction. *ACS Nano* **2019**, *13*, 9907−9917.
(20) Castilla, S.; Terres, B.; Autore, M.; Viti, L.; Li, J.; Nikitin, A. Y.; Vangelidis, I.; Watanabe, K.; Taniguchi, T.; Lidorikis, E.; et al. Fast and Sensitive Terahertz Detection Ssing an Antenna-Integrated Graphene Pn Junction. *Nano Lett.* **2019**, *19*, 2765−2773.
(21) Vicarelli, L.; Vitiello, M. S.; Coquillat, D.; Lombardo, A.; Ferrari, A. C.; Knap, W.; Polini, M.; Pellegrini, V.; Tredicucci, A. Graphene Field-Effect Transistors as Room-Temperature Terahertz Detectors. *Nat. Mater.* **2012**, *11*, 865−871.
(22) Bandurin, D. A.; Svintsov, D.; Gayduchenko, I.; Xu, S. G. G.; Principi, A.; Moskotin, M.; Tretyakov, I.; Yagodkin, D.; Zhukov, S.; Taniguchi, T.; et al. Resonant Terahertz Detection Using Graphene Plasmons. *Nat. Commun.* **2018**, *9*, 5392.
(23) Gabor, N. M.; Song, J. C. W.; Ma, Q.; Nair, N. L.; Taychatanapat, T.; Watanabe, K.; Taniguchi, T.; Levitov, L. S.; Jarillo-Herrero, P. Hot Carrier−Assisted Intrinsic Photoresponse in Graphene. *Science* **2011**, *334*, 648.
(24) Konstantatos, G.; Badioli, M.; Gaudreau, L.; Osmond, J.; Bernechea, M.; de Arquer, F. P. G.; Gatti, F.; Koppens, F. H. L. Hybrid Graphene-Quantum Dot Phototransistors with Ultrahigh Gain. *Nat. Nanotechnol.* **2012**, *7*, 363−368.
(25) Efetov, D. K.; Shiue, R. J.; Gao, Y. D.; Skinner, B.; Walsh, E. D.; Choi, H.; Zheng, J. B.; Tan, C.; Grosso, G.; Peng, C.; et al. Fast Thermal Relaxation in Cavity-Coupled Graphene Bolometers with a Johnson Noise Read-Out. *Nat. Nanotechnol.* **2018**, *13*, 797−801.

(26) Shiue, R. J.; Gao, Y. D.; Wang, Y. F.; Peng, C.; Robertson, A. D.; Efetov, D. K.; Assefa, S.; Koppens, F. H. L.; Hone, J.; Englund, D. High-Responsivity Graphene-Boron Nitride Photodetector and Autocorrelator in a Silicon Photonic Integrated Circuit. *Nano Lett.* **2015**, *15*, 7288−7293.
(27) Mueller, T.; Xia, F. N. A.; Avouris, P. Graphene Photodetectors for High-Speed Optical Communications. *Nat. Photonics* **2010**, *4*, 297−301.
(28) Zeng, L. H.; Lin, S. H.; Li, Z. J.; Zhang, Z. X.; Zhang, T. F.; Xie, C.; Mak, C. H.; Chai, Y.; Lau, S. P.; Luo, L. B.; et al. Fast, Self-Driven, Air-Stable, and Broadband Photodetector Based on Vertically Aligned Ptse2/Gaas Heterojunction. *Adv. Funct. Mater.* **2018**, *28*, 1705970.
(29) Castilla, S.; Terrés, B.; Autore, M.; Viti, L.; Li, J.; Nikitin, A. Y.; Vangelidis, I.; Watanabe, K.; Taniguchi, T.; Lidorikis, E.; et al. Fast and Sensitive Terahertz Detection Ssing an Antenna-Integrated Graphene Pn Junction. *Nano Lett.* **2019**, *19*, 2765−2773.
(30) Freitag, M.; Low, T.; Martin-Moreno, L.; Zhu, W. J.; Guinea, F.; Avouris, P. Substrate-Sensitive Mid-Infrared Photoresponse in Graphene. *ACS Nano* **2014**, *8*, 8350−8356.
(31) Freitag, M.; Low, T.; Xia, F. N.; Avouris, P. Photoconductivity of Biased Graphene. *Nat. Photonics* **2013**, *7*, 53−59.
(32) Freitag, M.; Low, T.; Zhu, W. J.; Yan, H. G.; Xia, F. N.; Avouris, P. Photocurrent in Graphene Harnessed by Tunable Intrinsic Plasmons. *Nat. Commun.* **2013**, *4*, 1951.
(33) Castro Neto, A. H.; Guinea, F.; Peres, N. M. R.; Novoselov, K. S.; Geim, A. K. The Electronic Properties of Graphene. *Rev. Mod. Phys.* **2009**, *81*, 109−162.
(34) Dean, C. R.; Young, A. F.; Meric, I.; Lee, C.; Wang, L.; Sorgenfrei, S.; Watanabe, K.; Taniguchi, T.; Kim, P.; Shepard, K. L.; et al. Boron Nitride Substrates for High-Quality Graphene Electronics. *Nat. Nanotechnol.* **2010**, *5*, 722−726.
(35) Wang, L.; Meric, I.; Huang, P. Y.; Gao, Q.; Gao, Y.; Tran, H.; Taniguchi, T.; Watanabe, K.; Campos, L. M.; Muller, D. A.; et al. One-Dimensional Electrical Contact to a Two-Dimensional Material. *Science* **2013**, *342*, 614−617.
(36) Li, Z. Q.; Henriksen, E. A.; Jiang, Z.; Hao, Z.; Martin, M. C.; Kim, P.; Stormer, H. L.; Basov, D. N. Dirac Charge Dynamics in Graphene by Infrared Spectroscopy. *Nat. Phys.* **2008**, *4*, 532−535.
(37) Bolotin, K. I.; Sikes, K. J.; Hone, J.; Stormer, H. L.; Kim, P. Temperature-Dependent Transport in Suspended Graphene. *Phys. Rev. Lett.* **2008**, *101*, 096802.
(38) Heo, J.; Chung, H. J.; Lee, S. H.; Yang, H.; Seo, D. H.; Shin, J. K.; Chung, U. I.; Seo, S.; Hwang, E. H.; Das Sarma, S. Nonmonotonic Temperature Dependent Transport in Graphene Grown by Chemical Vapor Deposition. *Phys. Rev. B: Condens. Matter Mater. Phys.* **2011**, *84*, 035421.
(39) Hwang, E. H.; Adam, S.; Das Sarma, S. Carrier Transport in Two-Dimensional Graphene Layers. *Phys. Rev. Lett.* **2007**, *98*, 186806.
(40) Das Sarma, S.; Hwang, E. H. Density-Dependent Electrical Conductivity in Suspended Graphene: Approaching the Dirac Point in Transport. *Phys. Rev. B: Condens. Matter Mater. Phys.* **2013**, *87*, 035415.
(41) Sohier, T.; Calandra, M.; Park, C. H.; Bonini, N.; Marzari, N.; Mauri, F. Phonon-Limited Resistivity of Graphene by First-Principles Calculations: Electron-Phonon Interactions, Strain-Induced Gauge Field, and Boltzmann Equation. *Phys. Rev. B: Condens. Matter Mater. Phys.* **2014**, *90*, 125414.
(42) Ni, G. X.; McLeod, A. S.; Sun, Z.; Wang, L.; Xiong, L.; Post, K. W.; Sunku, S. S.; Jiang, B. Y.; Hone, J.; Dean, C. R.; et al. Fundamental Limits to Graphene Plasmonics. *Nature* **2018**, *557*, 530−533.
(43) Li, Q. Z.; Hwang, E. H.; Das Sarma, S. Disorder-Induced Temperature-Dependent Transport in Graphene: Puddles, Impurities, Activation, and Diffusion. *Phys. Rev. B: Condens. Matter Mater. Phys.* **2011**, *84*, 115442.
(44) Du, X.; Skachko, I.; Barker, A.; Andrei, E. Y. Approaching Ballistic Transport in Suspended Graphene. *Nat. Nanotechnol.* **2008**, *3*, 491−495.
(45) Betz, A. C.; Jhang, S. H.; Pallecchi, E.; Ferreira, R.; Feve, G.; Berroir, J. M.; Placais, B. Supercollision Cooling in Undoped Graphene. *Nat. Phys.* **2013**, *9*, 109−112.
(46) Song, J. C. W.; Reizer, M. Y.; Levitov, L. S. Disorder-Assisted Electron-Phonon Scattering and Cooling Pathways in Graphene. *Phys. Rev. Lett.* **2012**, *109*, 106602.
(47) Das Sarma, S.; Adam, S.; Hwang, E. H.; Rossi, E. Electronic Transport in Two-Dimensional Graphene. *Rev. Mod. Phys.* **2011**, *83*, 407−470.
(48) Hwang, E. H.; Das Sarma, S. Dielectric Function, Screening, and Plasmons in Two-Dimensional Graphene. *Phys. Rev. B: Condens. Matter Mater. Phys.* **2007**, *75*, 205418.
(49) Adam, S.; Hwang, E. H.; Galitski, V. M.; Das Sarma, S. A Self-Consistent Theory for Graphene Transport. *Proc. Natl. Acad. Sci. U. S. A.* **2007**, *104*, 18392−18397.
(50) Tan, Y. W.; Zhang, Y.; Bolotin, K.; Zhao, Y.; Adam, S.; Hwang, E. H.; Das Sarma, S.; Stormer, H. L.; Kim, P. Measurement of Scattering Rate and Minimum Conductivity in Graphene. *Phys. Rev. Lett.* **2007**, *99*, 246803.
(51) Ziegler, K. Minimal Conductivity of Graphene: Nonuniversal Values from the Kubo Formula. *Phys. Rev. B: Condens. Matter Mater. Phys.* **2007**, *75*, 233407.
(52) Stampfer, C.; Guttinger, J.; Hellmueller, S.; Molitor, F.; Ensslin, K.; Ihn, T. Energy Gaps in Etched Graphene Nanoribbons. *Phys. Rev. Lett.* **2009**, *102*, 056403.
(53) Han, M. Y.; Brant, J. C.; Kim, P. Electron Transport in Disordered Graphene Nanoribbons. *Phys. Rev. Lett.* **2010**, *104*, 056801.
(54) Ashcroft, N. W.; Mermin, N. D. *Solid State Physics*; Thomson Learning: Boston, 1976.
(55) Abdel-Rahman, M.; Al-Khalli, N.; Zia, M. F.; Alduraibi, M.; Ilahi, B.; Awad, E.; Debbar, N. Fabrication and Design of Vanadium Oxide Microbolometer. *AIP Conf. Proc.* **2016**, *1809*, 020001.
(56) Ma, Q.; Lui, C. H.; Song, J. C. W.; Lin, Y.; Kong, J. F.; Cao, Y.; Dinh, T. H.; Nair, N. L.; Fang, W.; Watanabe, K.; et al. Giant Intrinsic Photoresponse in Pristine Graphene. *Nat. Nanotechnol.* **2019**, *14*, 145−150.
(57) Fuhrer, M. S.; Medhekar, N. V. Dirac-Point Photocurrents Due to Photothermoelectric Effect in Non-Uniform Graphene Devices. 2019, arXiv:1905.05331. arXiv.org e-Print archive. http://arxiv.org/abs/1905.05331, DOI: 10.1038/s41565-020-0637-1 (accessed Apr. 9, 2020).
(58) Caldwell, J. D.; Kretinin, A. V.; Chen, Y. G.; Giannini, V.; Fogler, M. M.; Francescato, Y.; Ellis, C. T.; Tischler, J. G.; Woods, C. R.; Giles, A. J.; et al. Sub-Diffractional Volume-Confined Polaritons in the Natural Hyperbolic Material Hexagonal Boron Nitride. *Nat. Commun.* **2014**, *5*, 5221.
(59) Martin, J.; Akerman, N.; Ulbricht, G.; Lohmann, T.; Smet, J. H.; Von Klitzing, K.; Yacoby, A. Observation of Electron-Hole Puddles in Graphene Using a Scanning Single-Electron Transistor. *Nat. Phys.* **2008**, *4*, 144−148.
(60) Gabor, N. M.; Song, J. C. W.; Ma, Q.; Nair, N. L.; Taychatanapat, T.; Watanabe, K.; Taniguchi, T.; Levitov, L. S.; Jarillo-Herrero, P. Hot Carrier-Assisted Intrinsic Photoresponse in Graphene. *Science* **2011**, *334*, 648−652.
(61) Yan, H. G.; Xia, F. N.; Zhu, W. J.; Freitag, M.; Dimitrakopoulos, C.; Bol, A. A.; Tulevski, G.; Avouris, P. Infrared Spectroscopy of Wafer-Scale Graphene. *ACS Nano* **2011**, *5*, 9854−9860.
(62) Pop, E.; Varshney, V.; Roy, A. K. Thermal Properties of Graphene: Fundamentals and Applications. *MRS Bull.* **2012**, *37*, 1273−1281.
(63) Xia, F. N.; Mueller, T.; Lin, Y. M.; Valdes-Garcia, A.; Avouris, P. Ultrafast Graphene Photodetector. *Nat. Nanotechnol.* **2009**, *4*, 839−843.
(64) Gan, X. T.; Shiue, R. J.; Gao, Y. D.; Meric, I.; Heinz, T. F.; Shepard, K.; Hone, J.; Assefa, S.; Englund, D. Chip-Integrated Ultrafast Graphene Photodetector with High Responsivity. *Nat. Photonics* **2013**, *7*, 883−887.

https://dx.doi.org/10.1021/acsphotonics.0c00028
ACS Photonics 2020, 7, 1206−1215

(65) VonHaartman, M.; Ostling, M. *Low-Frequency Noise in Advanced Mos Devices*; Springer Netherlands: Heidelberg, 2007; pp 1−216.
(66) Mather, J. C. Bolometer Noise: Nonequilibrium Theory. *Appl. Opt.* **1982**, *21*, 1125−1129.
(67) Xie, C. Z.; Aziz, M.; Pusino, V.; Khalid, A.; Steer, M.; Thayne, I. G.; Sorel, M.; Cumming, D. R. S. Single-Chip, Mid-Infrared Array for Room Temperature Video Rate Imaging. *Optica* **2017**, *4*, 1498−1502.
(68) Furchi, M.; Urich, A.; Pospischil, A.; Lilley, G.; Unterrainer, K.; Detz, H.; Klang, P.; Andrews, A. M.; Schrenk, W.; Strasser, G.; et al. Microcavity-Integrated Graphene Photodetector. *Nano Lett.* **2012**, *12*, 2773−2777.
(69) Jariwala, D.; Davoyan, A. R.; Tagliabue, G.; Sherrott, M. C.; Wong, J.; Atwater, H. A. Near-Unity Absorption in Van Der Waals Semiconductors for Ultrathin Optoelectronics. *Nano Lett.* **2016**, *16*, 5482−5487.
(70) Insb Photovoltaic Detectors. https://www.hamamatsu.com/resources/pdf/ssd/p5968-060_etc_kird1039e.pdf (accessed Apr. 9, 2020).

https://dx.doi.org/10.1021/acsphotonics.0c00028
ACS Photonics 2020, 7, 1206−1215

Supporting Information for "Room Temperature Graphene Mid-Infrared Bolometer with a Broad Operational Wavelength Range"

Shaofan Yuan[†,∥], Renwen Yu[⊥,∥], Chao Ma[†], Bingchen Deng[†], Qiushi Guo[†], Xiaolong Chen[†,#], Cheng Li[†], Chen Chen[†], Kenji Watanabe[‡], Takashi Taniguchi[‡], F. Javier García de Abajo[,⊥,§], and Fengnian Xia*[,†]*

[†]Department of Electrical Engineering, Yale University, New Haven, Connecticut 06511, USA.

[⊥]ICFO-Institut de Ciencies Fotoniques, The Barcelona Institute of Science and Technology, 08860 Castelldefels, Barcelona, Spain.

[‡]National Institute for Materials Science, 1-1 Namiki, Tsukuba 305-0044, Japan.

[§]Institució Catalana de Recerca i Estudis Avançats (ICREA), Passeig Lluís Companys 23, 08010 Barcelona, Spain.

*Correspondence to: fengnian.xia@yale.edu; javier.garciadeabajo@nanophotonics.es.

[∥] These authors contributed equally to this work.

Contents

1. The measured graphene TCR based on four-probe method.

Four-probe transport characterizations were performed using an Agilent B1500A semiconductor analyzer in a Lakeshore cryogenic probe station. This approach eliminates the contribution from the contact. We calculate the temperature coefficient of graphene resistance as $TCR = (\Delta R/\Delta T)/R_0$, where $\Delta R = R(300\text{K}) - R(260\text{K})$ is the difference of resistance at 300 K and 260 K, ΔT = 300-260 = 40 K, and $R_0 = (R(300\text{K}) + R(260\text{K}))/2$. The calculated TCR is shown in the lower right inset of Fig. 1b.

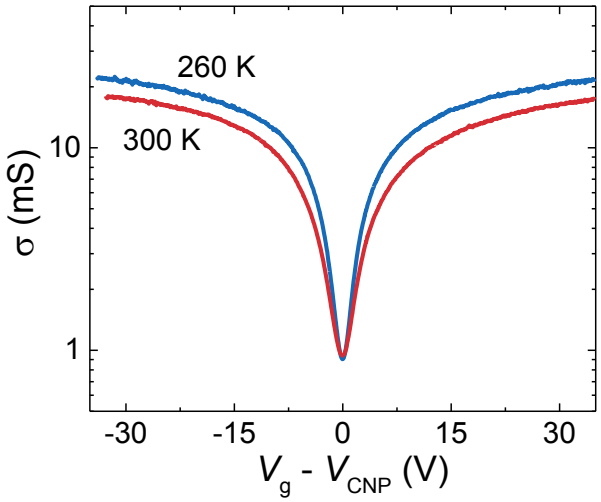

Figure S1: Measured conductivity of hBN-encapsulated graphene shown in Fig. 1b at 260 K and 300 K.

2. Transport model of hBN-encapsulated graphene device

In order to simulate transport over a broad range of doping levels, we adopt the theoretical model reported in Ref. 1, where a Gaussian distribution of fluctuating local potential (with standard deviation *s*) around the CNP is assumed. When the doping level is high enough (uniform doping regime, see details in Section 1A below), only one type of charge carrier contributes to the transport. The dominant scattering channels of the diffusive transport come from impurities[2, 3] and phonons[4, 5]. Here, we take both short- and long-range impurities into account. Regarding electron-phonon coupling, we include acoustic phonons, optical phonons at the Γ point, and intervalley optical A_1' phonons at the K point, as detailed in Ref. 5. Instead, when the doping level is low (electron-hole puddle regime, see details in Section 1B below), electron-hole puddles are formed[6, 7]. In this regime, both electrons and holes contribute to the electric current under external electric bias. The activated transport across potential fluctuations is then accompanied by regular diffusive transport[1].

A. Uniform doping regime

In this regime, the energy-dependent scattering time $\tau_i^{(u)}(\varepsilon_{\mathbf{k}})$ for u-type (u =1 for short-range impurities, and u = 2 for long-range impurities) impurity scattering is given according to Ref. 3 by

$$\frac{1}{\tau_i^{(u)}\left(\varepsilon_{\mathbf{k}}\right)} = \frac{2\pi}{A\hbar}\sum_{\mathbf{k}'} n_i^{(u)}\left|V_{\mathbf{k}\mathbf{k}'}^{(u)}\right|^2\left(1-\cos\theta_{\mathbf{k}\mathbf{k}'}\right)\delta\left(\varepsilon_{\mathbf{k}}-\varepsilon_{\mathbf{k}'}\right),$$

where A is the graphene area, $n_i^{(u)}$ is the u-type impurity density, $V_{\boldsymbol{k}\boldsymbol{k}'}^{(u)}$ is the disorder potential associated with the u-type impurity, $\theta_{\boldsymbol{k}\boldsymbol{k}'}$ is the scattering angle between the incoming and outgoing wave vectors $\boldsymbol{k}$ and $\boldsymbol{k}'$, and $\varepsilon_{\mathbf{k}} = \hbar v_F|\boldsymbol{k}|$ is the electronic energy with v_F the Fermi velocity in graphene.

For short-range impurity scattering (with impurity density $n_i^{(1)}$), we have[3]

$$\left|V_{\mathbf{kk}'}\right|^2 = V_0 \frac{1+\cos\theta_{\mathbf{kk}'}}{2},$$

where V_0 is the strength of the short-range impurity.

Instead, for long-range impurities (with impurity density $n_i^{(2)}$), we have[3]

$$\left|V_{\mathbf{kk}'}\right|^2 = \left|\frac{2\pi e^2 \exp(-qd)}{\epsilon_b q \epsilon(q)}\right|^2 \frac{1+\cos\theta_{\mathbf{kk}'}}{2},$$

where $q = |\boldsymbol{q}| = |\boldsymbol{k}' - \boldsymbol{k}|$, d is the separation distance between the graphene sheet and the impurities, ϵ_b is the background dielectric constant, and $\epsilon(q) \equiv \epsilon(q, T_e)$ is the static dielectric function of graphene[8].

Following previously published work[5], we write the energy-dependent scattering time $\tau_p^{(b)}(\varepsilon_{\boldsymbol{k}}^l)$ for the b-type phonon scattering as

$$\frac{1}{\tau_{\mathrm{p}}^{(b)}\left(\varepsilon_{\mathbf{k}}^l\right)} = \sum_{\mathbf{k}',l'} P_{\mathbf{kk}',b}^{ll'} \frac{1-f\left(\varepsilon_{\mathbf{k}'}^{l'}\right)}{1-f\left(\varepsilon_{\mathbf{k}}^l\right)}\left(1-\cos\theta_{\mathbf{kk}'}\right),$$

where $\varepsilon_{\boldsymbol{k}}^l = l\hbar v_{\mathrm{F}}|\boldsymbol{k}|$, with $l = \pm 1$ the band index, $f(\varepsilon_k) = 1/\{[\exp((\varepsilon_k - \mu)/k_B T_e)] + 1\}$, with T_{e} the electron temperature and μ the chemical potential, denotes the Fermi-Dirac distribution, and $P_{\boldsymbol{kk}',b}^{ll'}$ is the electron-phonon (b-type) scattering probability given by[5]

$$P_{\mathbf{kk}',b}^{ll'} = \frac{2\pi}{\hbar}\left|g_{\mathbf{kk}',b}^{ll'}\right|^2 \left\{n\left(\omega_{\mathbf{q},b}\right)\delta\left(\varepsilon_{\mathbf{k}'}^{l'} - \varepsilon_{\mathbf{k}}^l - \hbar\omega_{\mathbf{q},b}\right) + \left[n\left(\omega_{\mathbf{q},b}\right)+1\right]\delta\left(\varepsilon_{\mathbf{k}'}^{l'} - \varepsilon_{\mathbf{k}}^l + \hbar\omega_{\mathbf{q},b}\right)\right\}.$$

Here $\boldsymbol{q} = \boldsymbol{k}' - \boldsymbol{k}$, $n(\omega_q)=1/\left[\exp(\hbar\omega_q/k_BT_l)-1\right]$, with T_l the lattice temperature, is the Bose-Einstein distribution, and $g^{ll'}_{\boldsymbol{kk}',b}$ is defined as[5]

$$g^{ll'}_{\mathbf{kk}',b} = \sqrt{\frac{\hbar}{A\rho\omega_{\mathbf{q},b}}} L^{ll'}_{\mathbf{kk}',b},$$

where ρ is the mass density of graphene, and the matrix elements $L^{ll'}_{\boldsymbol{kk}',b}$ for b-type phonons are listed in Eqs. (16-21) of Ref. 5 with relevant coupling constants obtained by density functional theory (DFT) calculations (see Table IV therein). In more detail, those constants are the acoustic gauge field β_{A}, the optical gauge field β_{O} for the optical phonons at the Γ point, the optical gauge field β_{K} for intervalley optical A_1' phonons at the K point, the effective sound velocity v_{A}, the optical phonon energy $\hbar\omega_O$, and the A_1' phonon energy $\hbar\omega_{\mathrm{A}_1'}$.

Then the DC conductivity of graphene can be computed as[5]

$$\sigma = \frac{e^2 v_{\mathrm{F}}^2}{2}\int d\varepsilon D(\varepsilon)\tau(\varepsilon)\left(-\frac{\partial f(\varepsilon)}{\partial\varepsilon}\right), \tag{1}$$

where $D(\varepsilon) = 2|\varepsilon|/\pi(\hbar v_F)^2$ is the electronic density of states in graphene, including spin and valley degeneracies, and the total scattering time $\tau(\varepsilon)$ is given by Matthiessen's rule,

$$\frac{1}{\tau(\varepsilon)} = \sum_u \frac{1}{\tau_{\mathrm{i}}^{(u)}(\varepsilon)} + \sum_b \frac{1}{\tau_{\mathrm{p}}^{(b)}(\varepsilon)}.$$

B. Electron-hole puddle regime

In the regime close to the CNP, transport contains two components: an activated transport combined with a regular diffusive transport, with contributions from both electrons and holes. Here,

we follow the theory described in Ref. 1. For the regular diffusive transport part, the conductivities σ_e and σ_h are given by Eq. (1) in the main text for electron and hole puddles, respectively, but with a modified density of states[1]

$$D_e(\varepsilon) = \frac{2}{\pi(\hbar v_F)^2}\left[\frac{\varepsilon}{2}\mathrm{erfc}\left(-\frac{\varepsilon}{\sqrt{2}s}\right) + \frac{s}{\sqrt{2\pi}}\exp\left(-\frac{\varepsilon^2}{2s^2}\right)\right]$$

for electrons and $D_h(\varepsilon) = D_e(-\varepsilon)$ for holes, where erfc(x) is the complementary error function. The modified chemical potential is then obtained by imposing charge conservation.

The activated transport conductivities are then given by[1]

$$\sigma_e^{(a)} = \sigma_e \exp\left[(E_F - V)/k_B T_e\right],$$
$$\sigma_h^{(a)} = \sigma_h \exp\left[(V - E_F)/k_B T_e\right],$$

where E_F is the Fermi energy relative to the Dirac point and V is the fluctuation potential, the distribution of which follows a Gaussian form

$$P(V) = \frac{1}{\sqrt{2\pi s^2}}\exp\left(-\frac{V^2}{2s^2}\right).$$

In fact, the standard deviation s can be calculated as[1, 6]

$$s^2 = 2\pi n_i^{(2)} e^4 \int \left|\frac{\exp(-kd)}{\epsilon_b k \epsilon(k)}\right|^2 kdk.$$

From here, we obtain the total conductivity for a 2D binary mixture of two components σ_1 and σ_2, corresponding to electron and hole puddles, respectively, as[1]

$$\sigma_{\mathrm{eh}} = \left(p - \frac{1}{2}\right)(\sigma_1 - \sigma_2) + \sqrt{\left(p - \frac{1}{2}\right)^2 (\sigma_1 - \sigma_2)^2 + \sigma_1 \sigma_2}, \quad (2)$$

where

$$\sigma_1 = \frac{1}{p}\int_{-\infty}^{E_{\mathrm{F}}} \left(\sigma_{\mathrm{e}} + \sigma_{\mathrm{e}}^{(a)}\right) P(V)\, dV,$$
$$\sigma_2 = \frac{1}{q}\int_{E_{\mathrm{F}}}^{+\infty} \left(\sigma_{\mathrm{h}} + \sigma_{\mathrm{h}}^{(a)}\right) P(V)\, dV,$$

with $p = -\int_{-\infty}^{E_F} P(V)\, dV$ and $q = 1 - p$.

For the device discussed in the main text, we adopt the parameters β_A=4.97 eV, β_O=11.4 eV/Å, v_A=16.23 km/s, $\hbar\omega_O$= 0.2 eV, $\hbar\omega_{A_1'}$ = 0.15 eV, d = 1 Å, $n_i^{(1)}V_0^2$= 4×10^{-3} (eV·Å)^2, $n_i^{(2)}$= 3.8×10^{10} cm^{-2}, and β_k= 14 eV/Å. Note that only d, $n_i^{(1)}V_0^2$, and $n_i^{(2)}$ are fitting parameters, used to match the hole branch of the measured transport results shown in Fig. 1b of the main manuscript through Eq. (2), whereas other parameters are obtained from DFT calculations.[5] Then, we use those parameters in Eq. (2) to obtain the theoretical results in Fig. 2 of the main manuscript. Note that Eq. (2) reduces to Eq. (1) in the metallic regime. Also using the same parameters, the scattering strengths Γ shown in Fig. 1c, d of the main manuscript are evaluated at the chemical potential μ (i.e., $\Gamma = \hbar/\tau_{\mathrm{i}}^{(u)}(\mu)$ and $\hbar/\tau_{\mathrm{p}}^{(b)}(\mu)$ for impurity and phonon scattering channels, respectively), while the calculated standard deviation s is shown in Fig. 1e.

3. Extraction of the contact resistance using a four-probe configuration

We extract the contact resistivity ρ_c using a standard four-probe configuration[9]. The resulting ρ_c is plotted as a function of V_g in Fig. S1[9]. In the six measured devices, the contact resistivity ρ_c falls within a range of 500 to 1000 Ω·μm at 300 K for E_F = -160 meV. (Fig. S1a). Note that ρ_c is not sensitive to temperature in this edge contact configuration.[10] Moreover, the temperature of the metal electrodes does not increase considerably under infrared illumination in our experiment because of its large thermal conductance.[11] As a result, the temperature dependence of ρ_c does not leads to a noticeable photoresponse.

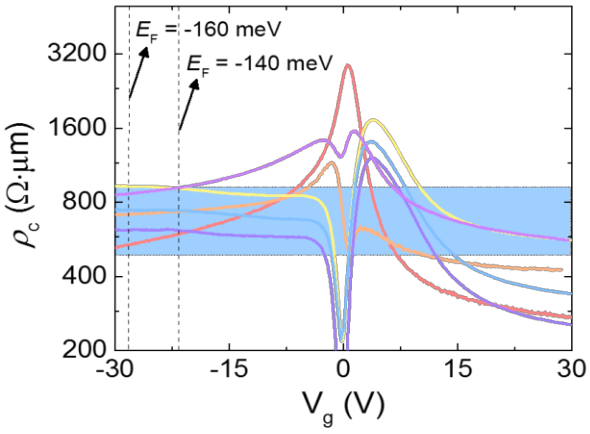

Figure S2: Contact resistivity measured in six samples as a function of gate voltage V_g.

4. Photoresponsivity and speed characterizations

The photocurrent measurements were performed using a lock-in amplifier technique in a nitrogen-purged stage (model HFS600E-PB4 from Linkam Scientific Instruments) mounted on a Bruker Hyperion microscope. The schematic of the measurement setup is shown in the Fig. S3 (see below). A 3.4 μm helium-neon laser (Model R-32172 from Research Electro-Optics) and 5.0, 7.7 and 12 μm quantum cascade lasers (Model HHL-306, Model HHL-304, and Model sbcw7971 DN from ALPES Lasers, respectively) were used to characterize the responsivity of our devices. The laser beams were modulated using an optical chopper (Thorlabs MC2000) at a modulation frequency fm up to 10 kHz, and then focused on our device using a Cassegrain objective (15×, N.A.=0.4). Our device output signal was fed into a low noise preamplifier (Femto DLPCA-200). The output voltage signal of the pre-amplifier was connected to a lock-in amplifier (Stanford Research SR830), and the generated photocurrent $I_{ph} = 2\pi\sqrt{2}V_{ph}/(4G_{gain})$ was recorded in reference to the modulation frequency (f_m = 980 Hz if not specified), where V_{ph} is the output voltage of the lock-in amplifier and G_{gain} = 1,000 V/A is the gain of the pre-amplifier. In the above equation, the factor of $2\sqrt{2}$ is due to the difference between peak-to-peak magnitude and root-mean-square magnitude acquired by the lock-in amplifier; and the factor of $4/\pi$ is the amplitude of the Fourier component of the fundamental sine-wave of the square wave produced due to chopping.

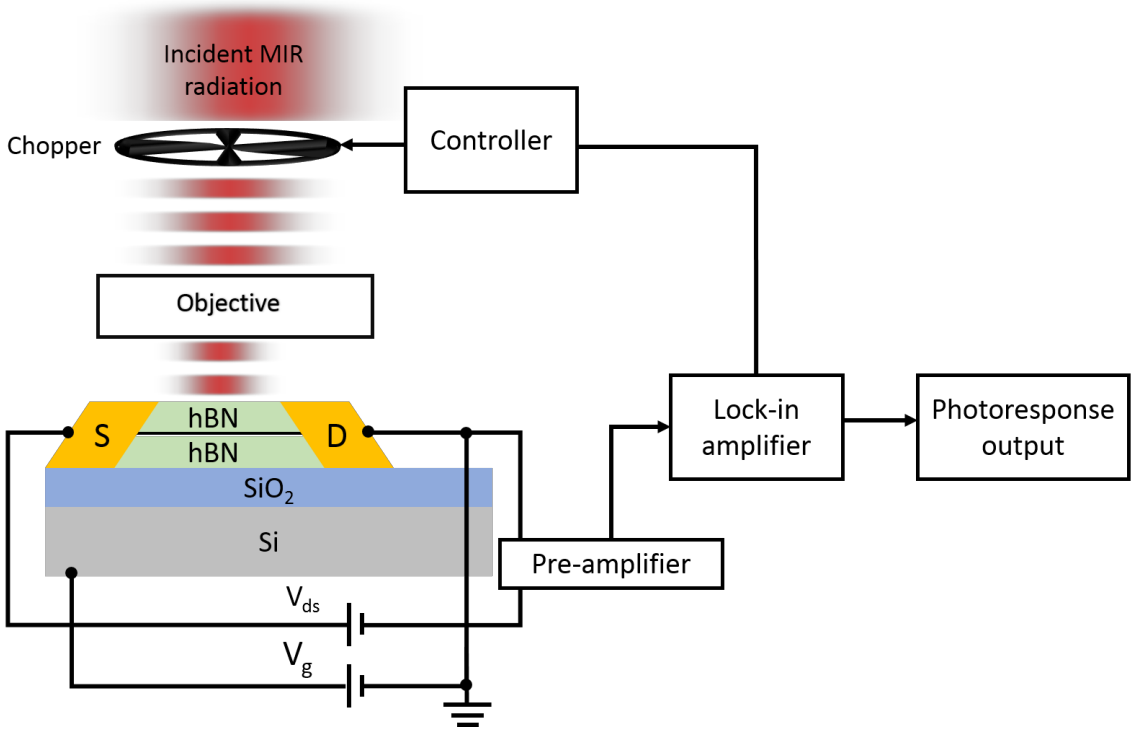

Figure S3: Schematic of our mid-infrared photocurrent measurement setup.

Note that the modulation frequency f_m of incident light could be tuned from 20 Hz to 1 kHz using a Thorlabs chopper MC1F10, and from 200 Hz to 10 kHz using a Thorlabs chopper MC1F100. The measured photocurrent responses in these two ranges were normalized to the photocurrent measured at 980 Hz and plotted in Fig. 5 of the main text.

We assumed isotropic in-plane Gaussian profiles for the incident light intensity S_{in} to calculate the power incident on the device (P_{dev}) based on $P_{dev}=\iint S_{in}(x,y)\,dxdy$. We used a rectangular gold reflector and a built-in mercury cadmium telluride (MCT) detector in Hyperion 2000 to determine the specific central positions and spatial profiles of the infrared light spot using a conventional knife-edge beam profile measurement scheme. First, we moved the reflector to achieve a half-maximum reflected power to pinpoint the central position of the light spot, $x_0 = 0$. Then, we recorded the position x_{half} at which a quarter of the maximum power was reflected. Based on the

Gauss error function erf ($x_{half}/\sqrt{2}\sigma$) = 0.5, the standard deviations σ of the Gaussian distributions were calculated to be 5.1, 7.2, 14 and 33 μm for 3.4, 5.0, 7.7 and 12 μm laser spots, respectively. The incident light intensity profiles were calibrated right after each photocurrent measurement, and may slightly differ when the light path is adjusted in different measurements.

The total incident power under the Cassegrain objective was measured to be 50, 180, 600 and 400 μW for 3.4, 5.0, 7.7 and 12 μm lasers, respectively, using an optical power meter console. Based on the total incident power, standard deviation of the Gaussian distribution, and the size of our device, we estimated P_{dev} to be 16, 30, 30 and 3.6 μW at 3.4, 5.0, 7.7 and 12 μm, respectively in photocurrent measurements. The measured extrinsic responsivities were calculated using $R_{ex} = I_{ph}/P_{dev}$.

For the IR photoresponse measurements at 80 K, the Linkam stage was cooled by liquid nitrogen (LN_2). By controlling the flow rate of LN_2 and the electrical current in the heater, the sample temperature could be kept at 80 K.

5. Photocurrent measured at 80 K and 300 K

The performance of the graphene photodetectors at 80 K and 300 K are summarized in the Fig. S4 (see below). At 80 K, the general properties are very similar to those at room temperature, indicating the same mechanism of photocurrent generation. We understand that the improvements of performance at 80 K are mainly due to the enhanced thermal isolation at lower temperatures. Note that at cryogenic temperatures both in-plane thermal conduction and out-of-plane thermal coupling are significantly reduced[12-15], which leads to an enhanced temperature elevation $\Delta T_{e/l}$ upon external light irradiation. According to Eq. (1) of the main manuscript, a larger photocurrent is thus expected.

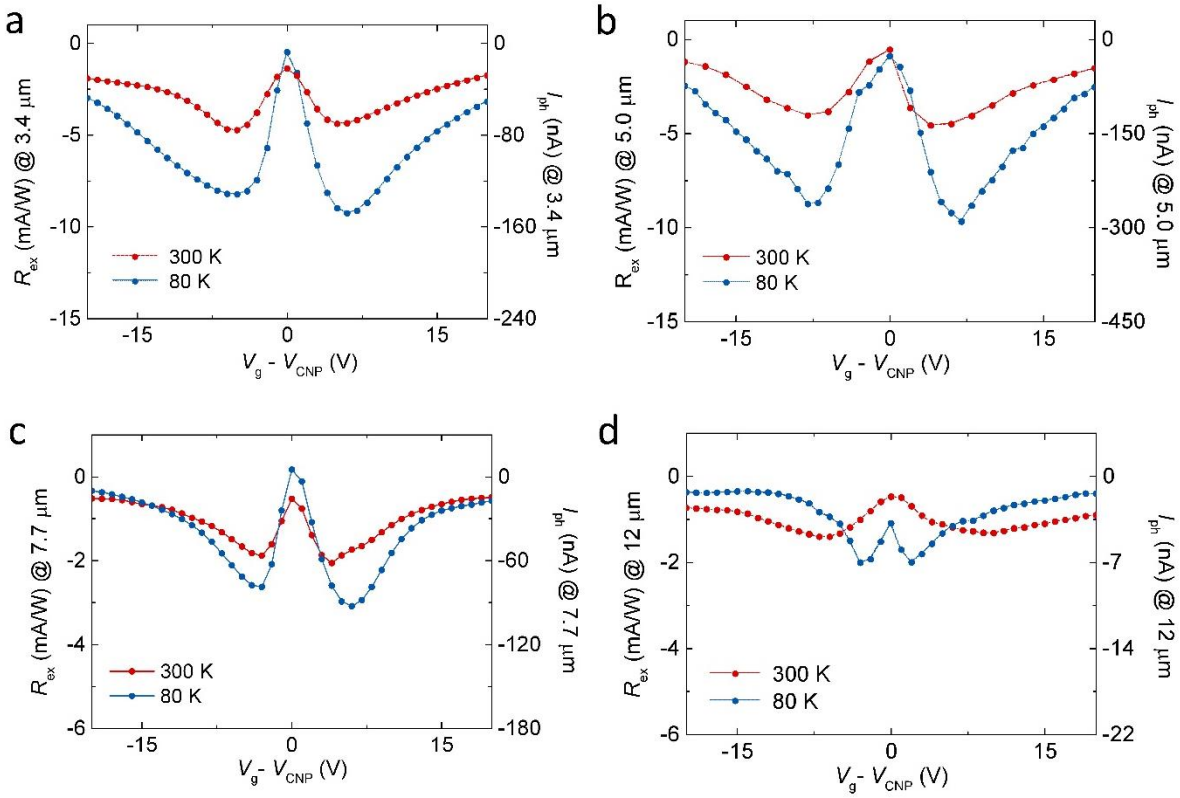

Figure S4: Extrinsic responsivity and photocurrent measured at 3.4 (a), 5.0 (b), 7.7 (c) and 12 (d) µm at 80 K (blue) and 300 K (red).

6. Spatially-resolved photocurrent scanning measurement at 1.3 μm

We characterize the two-terminal hBN-encapsulated graphene bolometer at 1.3 μm in a spatial-resolved photocurrent scanning scheme[16]. A piezoelectric mirror adjustor is used to scan the light spot over the device while the photocurrent I_{ph} is collected using a lock-in amplifier (see schematic of this photocurrent scanning setup in Fig. S5a). A reflection mapping image of the device (acquired using a 532 nm laser) is shown in Fig. 5b. When we focus the light spot at the center of the channel, the photocurrent shows a similar gate-voltage dependence at a source-drain bias of 0.5 V (Fig. S5c) as that shown in the main text. Additionally, when the light spot is scanned over the device, the photocurrent mapping shows a near-uniform photo-response across the channel at all four gate biases (-18, -8, 12, and 22 V). The same polarity of the photocurrent (always negative) in the entire channel indicates that the photo-thermoelectric component contributed by the graphene-metal junction is negligible in our devices.[17]

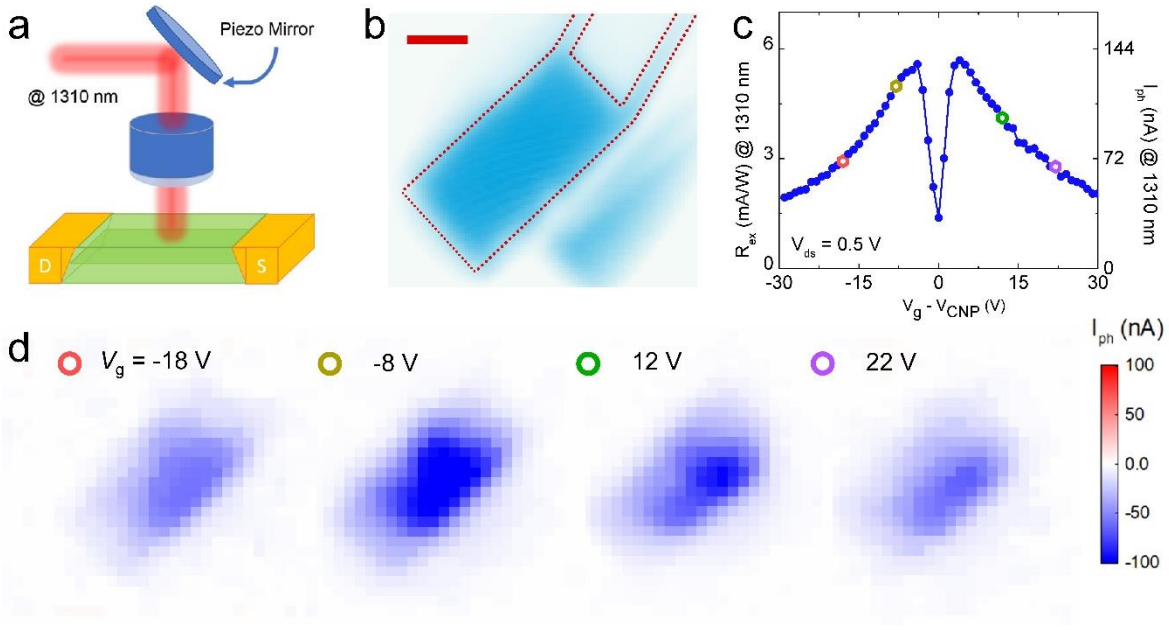

Figure S5: Photocurrent scanning measurement at 1.3 µm. (a) Schematic of photocurrent scanning measurement setup. **(b)** Refection image of the device acquired at 532 nm. Scale bar: 3.6 µm. The red-dotted lines indicate the edges of the measured device. **(c)** I_{ph}-V_g dependence at 1.3 µm with V_{ds} = 0.5 V. **(d)** Photocurrent scanning measurements at different voltages V_g = -18, -8, 12, and 22 V. In c and d, circles of different colors correspond to different values of V_g.

7. Performance variation among devices and the dependence of responsivity on carrier mobility

We measured the photoresponse in two additional devices, in which the absolute photoresponse is slightly smaller than what is reported in Fig. 4. The results are summarized in Table S1 and Fig. S6 (see below). When we estimate the mobility at a carrier density of $1.8\times10^{12}/cm^2$ in these two-terminal devices, we assume a contact resistance of 1000 Ω·μm. The source-drain bias voltage is set to 0.5 V in photocurrent measurements.

At small source-drain bias (far from the saturation regime), the normalized extrinsic responsivity (photocurrent divided by the power on the device) linearly depends on the electric field in the device. For D1 (the device shown in the main text) and D2, the widths are very different and this could lead to some error in the estimate of the power on the devices. Moreover, in D1 and D2 the two-terminal mobilities are relatively close. It is also hard to compare the performance of D1 and D2.

For D1 and D3, both of them have relatively large device area, which makes the estimate of the power on the devices more accurate. Moreover, the mobility of D3 is lower and the intrinsic mobility is only 8,100 $/cm^2/(V\cdot s)$ even if we assume a contact resistance of 1,000 Ω·μm. As a result, we can confidently conclude that D1 has a mobility higher than that of D3. Since D3 is 9 μm long and D1 is 6 μm long, the electric field in D1 is 1.5 times as large as that of D3 at the same bias voltage. As a result, D1 is expected to have a responsivity 1.5 times as large as that of D3 if their carrier mobility is the same. However, as shown in Table S1, the responsivity of D1 is about 3 times as large as that of D3, implying that a higher mobility does improve the device performance.

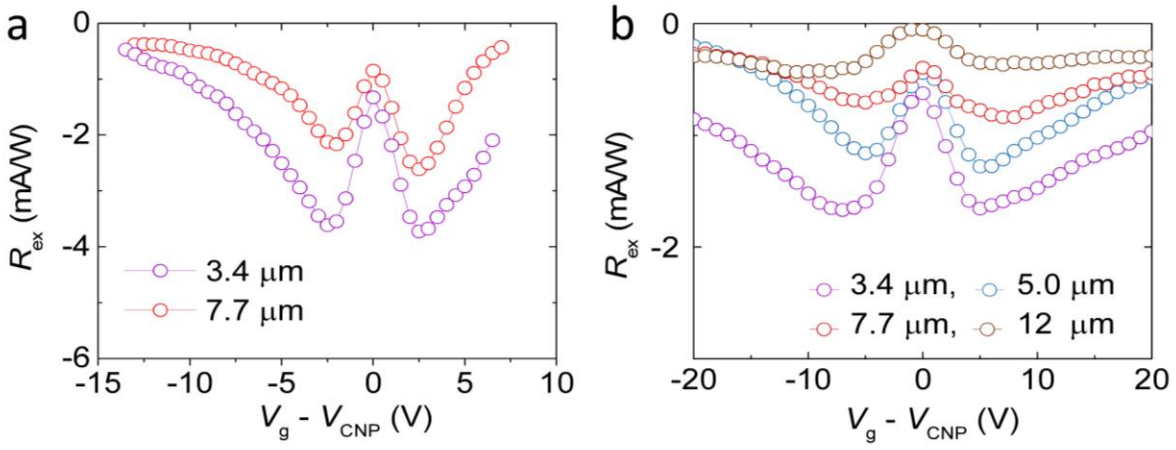

Figure S6: Extrinsic responsivity of samples D2 (a) and D3 (b) at mid-infrared wavelengths.

Table S1: Summarized properties of D1, D2, and D3.

	D1	D2	D3
Length×Width (μm^2)	6×10.5	6×3	9×13
Mobility ($cm^2/(V \cdot s)$)	22000	31000	8100
R_{ex} at 7.7 μm (mA/W)	2.1	2.6	0.84
R_{ex} at 3.4 μm (mA/W)	5.1	3.7	1.7

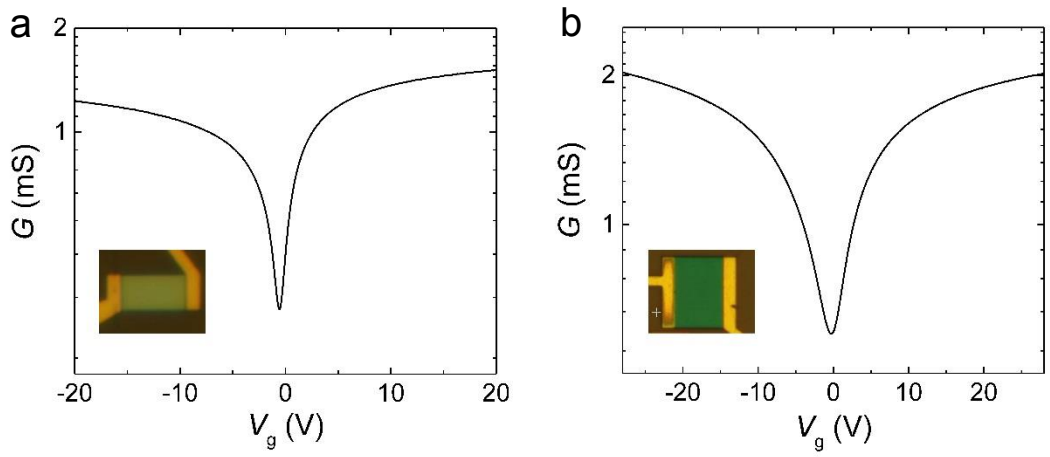

Figure S7: Conductance of D2 (a) and D3 (b) as a function of gate voltage V_g. In these devices, the conductance includes the contribution from the contact.

Besides the experimental results shown above, theory can also help us understand the effect of mobility on bolometric performance. In our high-quality graphene samples, the mobility is mainly affected by long-range, charged impurity scattering[9]. In the Fig. S8 (see below), we show the dependence of $d\sigma/dT$ on gate voltage at 300 K (σ is the conductivity) at different charged impurity concentrations. The photoresponse is directly related to $d\sigma/dT$, as shown in Eq. (1) of the main text. Here $n_i^{(1)}$ and $n_i^{(2)}$ represent the concentrations of short and long range scatterers, respectively.

From Fig. S8, it is clear that the photoresponse becomes weaker if the scatterer concentration is higher. Moreover, long-range scatterers (e.g., charged impurities) have a stronger effect. In devices with lower mobility, the concentration of long-range scatterers is usually higher and a weaker photoresponse is expected.

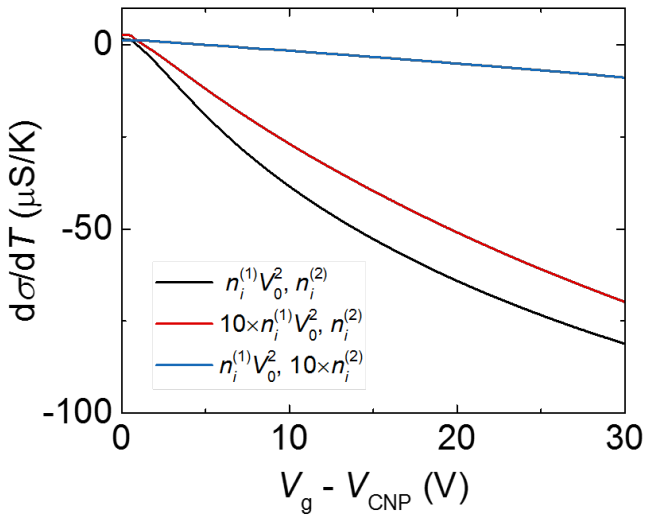

Figure S8: Temperature derivative of the conductivity dσ/dT at room temperature for different scatterer concentrations, $n_i^{(1)}$ (short-range scatterer concentration) and $n_i^{(2)}$ (long-range scatterer concentration). The black curve represents dσ/dT as calculated using values of $n_i^{(1)}$ and $n_i^{(2)}$ provided at the end of Section 2B.

Regarding devices made from graphene on oxide, we have not performed measurements on them in this work. However, one of the authors (F.X.) has previously published detailed studies of photoresponse in devices made from graphene on oxide within the visible wavelength range[18]. In those devices, the photoresponse properties are distinctively different from what we report in this work. The main reason is because the scattering mechanisms are very different, which leads to much smaller mobility (~3,000 $cm^2/(V \cdot s)$) and a much weaker dependence of the conductivity on temperature. As a result, the photoresponsivity is much smaller: only 0.25 mA/W for an incidence wavelength of 690 nm. We expect that the responsivity will be much smaller than 0.25 mA/W for graphene on oxide in the mid-infrared, because electron and hole puddles are abundant in that system and those puddles should further reduce absorption of low-energy photons.

8. Photocurrent model in the hBN/graphene/hBN heterostructure

In our system, the photocurrent results from the change in the electrical conductivity due to the temperature variation produced by the external illumination. Therefore, we first obtain the temperature variation to estimate the photocurrent using Eq. (2). Here, we adopt a two-temperature model[19-21] to characterize both the electron and lattice temperatures, T_e and T_l, the temporal evolution of which follow the equations[16]

$$\begin{aligned} C_e \frac{dT_e}{dt} &= P_{abs} - S_a H\left(T_e, T_l\right), \\ C_l \frac{dT_l}{dt} &= S_a H\left(T_e, T_l\right) - S_a B\left(T_l, T_s\right), \end{aligned} \tag{3}$$

where C_e and C_l are the electron and lattice heat capacities, respectively, T_s = 300 K is the ambient temperature, P_{abs} is the absorbed power, and S_a denotes the active area of graphene, incorporating the diffusive cooling pathway to the leads. Here, we take $B(T_l, T_s) = \kappa(T_l - T_s)$ to represent heat dissipation to the environment with a coupling coefficient κ =4×10^5 W/(K·m^2)[22, 23]. Additionally, $H(T_e, T_l)$ accounts for electron-phonon cooling in our system, given by[24]

$$\begin{aligned} H\left(T_e, T_l\right) = \frac{2\pi}{A\hbar} \sum_{\mathbf{q},b} \sum_{\mathbf{k},l} \sum_{\mathbf{k}',l'} \left(\varepsilon_{\mathbf{k}'}^{l'} - \varepsilon_{\mathbf{k}}^{l}\right) \left| g_{\mathbf{k}\mathbf{k}',b}^{ll'} \right|^2 \left[f\left(\varepsilon_{\mathbf{k}'}^{l'}\right) - f\left(\varepsilon_{\mathbf{k}}^{l}\right) \right] \\ \times \left[n\left(\omega_{\mathbf{q},b}, T_l\right) - n\left(\omega_{\mathbf{q},b}, T_e\right) \right] \delta_{\mathbf{k}',\mathbf{k}+\mathbf{q}} \delta\left(\varepsilon_{\mathbf{k}'}^{l'} - \varepsilon_{\mathbf{k}}^{l} - \hbar\omega_{\mathbf{q},b}\right), \end{aligned}$$

in which all of the aforementioned three types of phonon modes are taken into consideration. We note that P_{abs} depends on temperature through both electrical Joule heating (i.e., the temperature dependence in the electrical conductivity of graphene given in Eq. (2)) and light absorption (the temperature dependence in the optical conductivity of graphene, here described in the local limit of the random phase approximation[19, 25]). As we show below, T_e and T_l are noticeably higher than T_s because of Joule heating.

Under CW illumination conditions, we have $dT_e/dt = dT_l/dt = 0$ in Eq. (3). This equation can be in fact self-consistently solved (incorporating the temperature dependence in P_{abs}) to give the variations of both electron and lattice temperatures with/without external illumination (the P_{abs} term), from which we obtain the variation in the electrical conductivity produced by the incident light, and thus the photocurrent associated with it.

According to Eq. (1) and the profile of $\partial\sigma/\partial T_{e/l}$ shown in Fig. 2b of the main text, we would expect a sign change in the photocurrent close to the CNP in the calculation. However, due to the large Joule heating power $V_{ds}^2 \times G$ produced by the external bias voltage V_{ds} even in the absence of external illumination, the electron and lattice temperatures are elevated to $T_e \approx 430$ K and $T_l \approx 350$ K, respectively, where $\partial\sigma/\partial T_{e/l} \approx 8\times10^{-7}$ and -4×10^{-6} S/K at the CNP. We note that because $|\partial\sigma/\partial T_l| \gg |\partial\sigma/\partial T_e|$, according again to Eq. (1) there would be no sign change in the calculated photocurrent close to the CNP if we consider the computed values of $\Delta T_{e/l}$, caused by light absorption, as shown in Fig. 4b of the main text.

9. Infrared absorption in the hBN/graphene/hBN heterostructure

We evaluate light absorption in our system based on a conventional transfer matrix method in Ref. [26]. The permittivities of hBN, silicon oxide, and silicon are taken from Ref. [27], Refs. [28, 29] , and Refs. [30, 31], respectively. We calculate the temperature dependent optical conductivity of graphene using the local limit of the random phase approximation[19, 25]. In Fig. S3, we present the calculated light absorption in graphene under normal incidence with 5 μm light. The absorption of graphene at the CNP is ~1.2 %. This is smaller than the absorption in intrinsic free-standing graphene, which is ~2.3%,[32] because of the reduction of the local field in the hBN-encapsulated structure. Note that a decrease in light absorption in graphene is found when increasing the doping level, which is mainly due to the suppression of interband transitions in graphene (Pauli blocking).[19, 33]

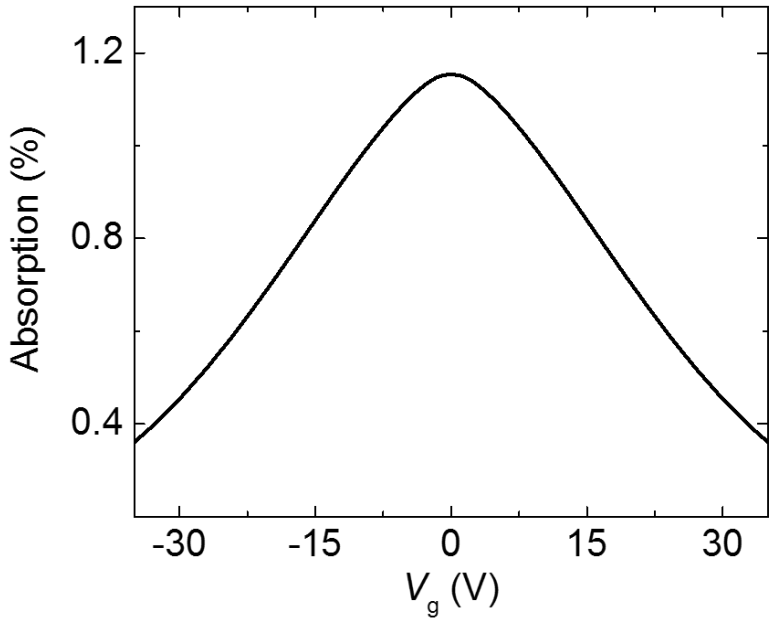

Figure S9: Calculated light absorption in hBN/graphene/hBN heterostructure at 5.0 μm.

10. Thermal dissipation analysis in the hBN/graphene/hBN heterostructure and frequency dependence of the photoresponse

We evaluate the dissipation to a thermal sink via graphene electrons and phonons considering the specific device dimensions (L = 6 μm, W = 10.5 μm in the device shown in Fig. 3). Heat dissipation via electron diffusion involves an electronic thermal conductivity of 80 W/(m·K) around room temperature at a high carrier density of 1.3 $\times 10^{13}$ cm^{-2} (Ref. 2). Note that this carrier density is much larger than the one at which a maximum responsivity is achieved in our experiment, n_h = 3.9×10^{11} cm^{-2}. Thus, we estimate an upper bound of electronic thermal conductance to electrodes (regarded as thermal sinks) of 4.7×10^{-7} W/K.[34] In fact, this is nearly two orders of magnitude smaller than the dissipation mediated by phonons around room temperature, and therefore, it is negligible in our thermal analysis; indeed, thermal dissipation via electron-phonon coupling in graphene highly depends on carrier density and contributes a thermal conductance of 1.5×10^{-5} W/K at $n_h = 3.9\times10^{11}$ /cm^2 (V_g-V_{CNP} = -6 V) and 7.3×10^{-5} W/K at $n_h = 1.9\times10^{12}$ /cm^2 (V_g-V_{CNP} = -30 V); these values are calculated based on the expressions detailed in *Supporting Information Section 8*. Eventually, heat in graphene phonons is dissipated to the environment mainly through the substrate; we take a thermal conductance of 2.5×10^{-5} W/K for this channel.[22, 23] Considering all these elements, the electronic heat is dissipated through a thermal sink with an equivalent thermal conductance G_{th} = 9.4 $\times10^{-6}$ W/K at V_g-V_{CNP} = -6 V and $G_{th} = 1.9\times10^{-5}$ W/K at V_g-V_{CNP} = -30 V.

Considering the dimensions of this device and the heat capacity of graphene (~8.5 J/(mol·K)),[35] we estimate the heat capacitance of graphene absorber C_h to be less than 2×10^{-13} J/K. This value overestimates the capacitance because the electronic heat capacitance is much smaller than the

phononic capacitance at room temperature[36]. We further estimate the response time of this graphene bolometer to be $\tau = C_h/G_{th}$ ~21 ns (i.e., ~47 MHz).

In experiments, the photocurrent is measured referenced to the modulation frequency f_m of incident light. As we change the modulation frequency from 20 Hz to 1 kHz and from 200 Hz to 10 kHz, no noticeable degradation in photo-response is observed. The measured photocurrent at 5.0 μm in these two ranges is normalized to the photocurrent measured at 980 Hz and plotted in Fig. 5. The normalized photocurrent at 7.7 and 12 μm is summarized in Figure S10. In short, our experiment and analysis show that the 3-dB cutoff frequency is well above 10 kHz and is independent of incident wavelengths in mid-infrared range.

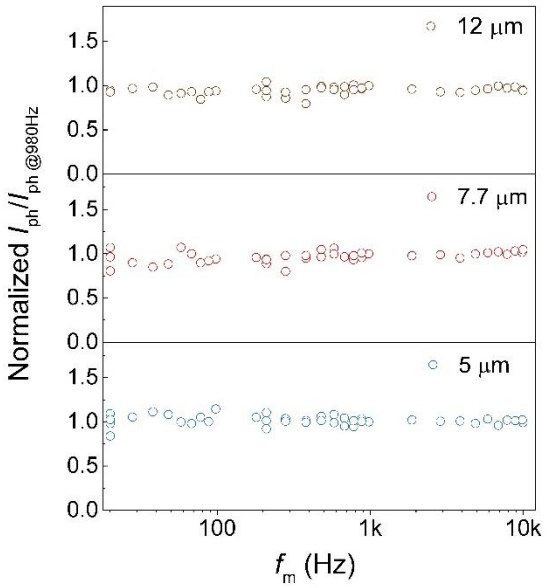

Figure S10: Normalized photocurrent as a function of modulation frequency f_m.

11.Noise current density measurement and calculation

The setup for noise spectral measurements was similar to that of the photocurrent characterization. In the noise measurement, the device was loaded into a shielded probe station without light excitation. The preamplifier converted noise current to noise voltage that could be measured by the lock-in amplifier with an equivalent noise bandwidth (ENBW). The ENBW was determined by the time constant T (300 mS) and slope (24 dB/oct) used in the measurement to be ENBW = $5/(65T)$ = 0.26 Hz[37]. The noise current density (S_I) was determined based on the expression $S_I = S_V/\text{ENBW}\times G$, where G is the gain of the preamplifier, S_V/ENBW is the output of the lock-in amplifier. The measured noise current density showed a clear $1/f$ dependence from 10 Hz to 10 kHz, and the measured noise current density was close to the theoretical limit at 10 kHz. This observation indicates that the $1/f$ noise only dominates at low frequencies below 10 kHz. As a result, we can rely on the theoretical high-frequency noise to calculate the noise equivalent power (NEP) of our device.

We consider Johnson noise, thermal-fluctuation noise, and shot noise to estimate the noise current density and NEP in our device.[13,38,39] Johnson noise originates from random thermal motion of electrons and results in a power spectral density given by $\frac{4k_BT_e}{R}$, where R is the resistance of the device.[38] Fluctuations in T_e (denoted δT_e) cause variations in resistance and current because of the presence of temperature-sensitive transport. This leads to thermal-fluctuation noise in our device.[32] The power spectral density of the latter is estimated by using the expression $\delta i^2 = \frac{4k_BT_e}{R} \times \frac{T_e(T_e-T_s)}{1+\omega^2\tau^2} \times \beta^2$, where ω is the measurement frequency, $\beta = \frac{dG}{dT}G^{-1} \sim 0.5$ %, and we have $\omega^2\tau^2 \ll 1$ in most applications[20, 40, 41]. Shot noise exists in mesoscopic resistors at a lower level than in tunneling junctions ($\delta i^2 \leq \sqrt{3/4}\, eI$, where I is the dark current)[39], and it vanishes in

macroscopic resistors, where the channel is longer than the electron-phonon interaction length[39]. In our device at high frequencies, we therefore have $\sqrt{\delta i^2} \leq \left[\frac{4k_B T_e}{R}(1 + T_e(T_e - T_s)\beta^2) + \sqrt{3/4}eI\right]^{1/2}$. Other contributions to the total noise current density in our device, such as fluctuations caused by environmental thermal radiation, are comparatively negligible.

The device shown in Fig. 3 has a conductance G = 2.2 mS at $V_g - V_{CNP}$ = -6 V and $T_e \approx 430$ K at V_{ds} = 0.5 V caused by Joule heating of the dark current. The above considerations allow us to estimate a noise current density $\sqrt{\delta i^2} \approx 16\ \mathrm{pA/Hz^{1/2}}$ in the device. Accordingly, the NEP is 3, 3.6, 7.5, and 11 nW/Hz$^{1/2}$ at 3.4, 5.0, 7.7, and 12 µm, respectively, as indicated in the main text.

The extrinsic responsivity and NEP at infrared wavelengths are summarized in Fig. S11.

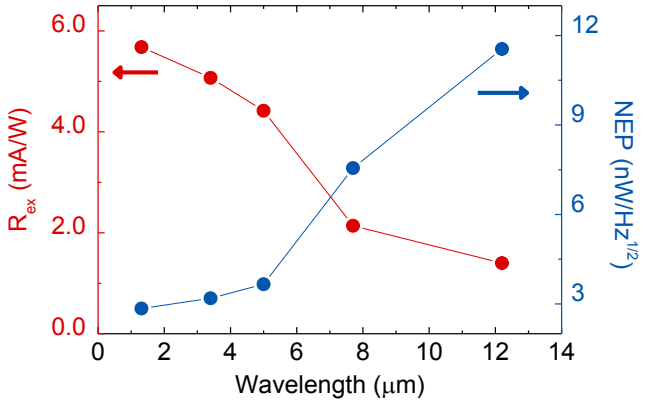

Figure S11: Extrinsic responsivity and NEP at different mid-infrared wavelengths

12. Comparison of device performance in different mid-infrared photodetectors

Table S2: Comparison of operational wavelength (λ), responsivity (R_{ex}), noise equivalent power (NEP) and operation speed of different devices

Device	λ (μm)	R_{ex}	NEP	Speed	ref
hBN-encapsulated graphene	1.3 - 12	5.1 mA/W at 3.4 μm, 1.4 mA/W at 12 μm	3 $nW/Hz^{1/2}$ at 3.4 μm, 11 $nW/Hz^{1/2}$ at 12 μm	≫ 47 MHz	this work
graphene	1.55	0.5 mA/W	-	40 GHz	[42]
graphene	0.69	0.25 mA/W	-	-	[18]
WS_2/Si	0.2-3	224 mA/W at 0.98 μm	-	22 kHz	[43]
Gr/$PdSe_2$/Ge	0.2−3	691 mA/W at 0.98 μm	-	10 kHz	[44]
Commercial microbolometer	11	-	10 $pW/Hz^{1/2}$	< 1 kHz	[45]
InSb	< 4.6	-	235 $pW/Hz^{1/2}$	~ 1 kHz	[46]

References

1. Li, Q. Z.; Hwang, E. H.; Das Sarma, S. Disorder-Induced Temperature-Dependent Transport in Graphene: Puddles, Impurities, Activation, and Diffusion. *Phys. Rev. B* **2011,** 84, 115442.

2. Hwang, E. H.; Adam, S.; Das Sarma, S. Carrier Transport in Two-Dimensional Graphene Layers. *Phys. Rev. Lett.* **2007,** 98, 186806.

3. Das Sarma, S.; Hwang, E. H. Density-Dependent Electrical Conductivity in Suspended Graphene: Approaching the Dirac Point in Transport. *Phys. Rev. B* **2013,** 87, 035415.

4. Hwang, E. H.; Das Sarma, S. Acoustic Phonon Scattering Limited Carrier Mobility in Two-Dimensional Extrinsic Graphene. *Phys. Rev. B* **2008,** 77, 115449.

5. Sohier, T.; Calandra, M.; Park, C. H.; Bonini, N.; Marzari, N.; Mauri, F. Phonon-Limited Resistivity of Graphene by First-Principles Calculations: Electron-Phonon Interactions, Strain-Induced Gauge Field, and Boltzmann Equation. *Phys. Rev. B* **2014,** 90, 125414.

6. Adam, S.; Hwang, E. H.; Galitski, V. M.; Das Sarma, S. A Self-Consistent Theory for Graphene Transport. *P. Nat. Acad. Sci. USA* **2007,** 104, 18392-18397.

7. Martin, J.; Akerman, N.; Ulbricht, G.; Lohmann, T.; Smet, J. H.; Von Klitzing, K.; Yacoby, A. Observation of Electron-Hole Puddles in Graphene Using a Scanning Single-Electron Transistor. *Nat. Phys.* **2008,** 4, 144-148.

8. Hwang, E. H.; Das Sarma, S. Dielectric Function, Screening, and Plasmons in Two-Dimensional Graphene. *Phys. Rev. B* **2007,** 75, 205418.

9. Dean, C. R.; Young, A. F.; Meric, I.; Lee, C.; Wang, L.; Sorgenfrei, S.; Watanabe, K.; Taniguchi, T.; Kim, P.; Shepard, K. L.*, et al.* Boron Nitride Substrates for High-Quality Graphene Electronics. *Nat. Nanotechnol.* **2010,** 5, 722-726.

10. Wang, L.; Meric, I.; Huang, P. Y.; Gao, Q.; Gao, Y.; Tran, H.; Taniguchi, T.; Watanabe, K.; Campos, L. M.; Muller, D. A.*, et al.* One-Dimensional Electrical Contact to a Two-Dimensional Material. *Science* **2013,** 342, 614-617.

11. Langer, G.; Hartmann, J.; Reichling, M. Thermal Conductivity of Thin Metallic Films Measured by Photothermal Profile Analysis. *Rev. Sci. Instrum.* **1997,** 68, 1510-1513.

12. Crossno, J.; Shi, J. K.; Wang, K.; Liu, X. M.; Harzheim, A.; Lucas, A.; Sachdev, S.; Kim, P.; Taniguchi, T.; Watanabe, K.*, et al.* Observation of the Dirac Fluid and the Breakdown of the Wiedemann-Franz Law in Graphene. *Science* **2016,** 351, 1058-1061.

13. Yigen, S.; Tayari, V.; Island, J. O.; Porter, J. M.; Champagne, A. R. Electronic Thermal Conductivity Measurements in Intrinsic Graphene. *Phys. Rev. B* **2013,** 87, 241411.

14. Tielrooij, K. J.; Hesp, N. C. H.; Principi, A.; Lundeberg, M. B.; Pogna, E. A. A.; Banszerus, L.; Mics, Z.; Massicotte, M.; Schmidt, P.; Davydovskaya, D.*, et al.* Out-of-Plane Heat Transfer in Van Der Waals Stacks through Electron-Hyperbolic Phonon Coupling. *Nat. Nanotechnol.* **2018,** 13, 41-46.

15. Hu, J. N.; Ruan, X. L.; Chen, Y. P. Thermal Conductivity and Thermal Rectification in Graphene Nanoribbons: A Molecular Dynamics Study. *Nano Lett.* **2009,** 9, 2730-2735.

16. Mueller, T.; Xia, F.; Freitag, M.; Tsang, J.; Avouris, P. Role of Contacts in Graphene Transistors: A Scanning Photocurrent Study. *Phys. Rev. B* **2009,** 79, 245430.

17. Tielrooij, K. J.; Massicotte, M.; Piatkowski, L.; Woessner, A.; Ma, Q.; Jarillo-Herrero, P.; Hulst, N. F. v.; Koppens, F. H. L. Hot-Carrier Photocurrent Effects at Graphene–Metal Interfaces. *Journal of Physics: Condensed Matter* **2015,** 27, 164207.

18. Freitag, M.; Low, T.; Xia, F. N.; Avouris, P. Photoconductivity of Biased Graphene. *Nat. Photonics* **2013,** 7, 53-59.

19. Yu, R. W.; Guo, Q. S.; Xia, F. N.; de Abajo, F. J. G. Photothermal Engineering of Graphene Plasmons. *Phys. Rev. Lett.* **2018,** 121, 057404.

20. Guo, Q. S.; Yu, R. W.; Li, C.; Yuan, S. F.; Deng, B. C.; de Abajo, F. J. G.; Xia, F. N. Efficient Electrical Detection of Mid-Infrared Graphene Plasmons at Room Temperature. *Nat. Mater.* **2018,** 17, 986-992.

21. Anisimov, S. I.; Kapeliovich, B. L.; Perel'man, T. L. Electron Emission from Metal Surfaces Exposed to Ultrashort Laser Pulses. *J. Exp. Theor. Phys.* **1973,** 66, 776.

22. Kim, Y. D.; Gao, Y. D.; Shiue, R. J.; Wang, L.; Aslan, O. B.; Bae, M. H.; Kim, H.; Seo, D.; Choi, H. J.; Kim, S. H.*, et al.* Ultrafast Graphene Light Emitters. *Nano Lett.* **2018,** 18, 934-940.

23. Bae, M. H.; Ong, Z. Y.; Estrada, D.; Pop, E. Imaging, Simulation, and Electrostatic Control of Power Dissipation in Graphene Devices. *Nano Lett.* **2010,** 10, 4787-4793.

24. Viljas, J. K.; Heikkila, T. T. Electron-Phonon Heat Transfer in Monolayer and Bilayer Graphene. *Phys. Rev. B* **2010,** 81, 245404.

25. Yu, R. W.; Manjavacas, A.; de Abajo, F. J. G. Ultrafast Radiative Heat Transfer. *Nat. Commun.* **2017,** 8, 2.

26. Yu, R.; Pruneri, V.; de Abajo, F. J. G. Resonant Visible Light Modulation with Graphene. *2016 Progress in Electromagnetics Research Symposium (PIERS)* **2016**, 4952-4952.

27. Caldwell, J. D.; Kretinin, A. V.; Chen, Y. G.; Giannini, V.; Fogler, M. M.; Francescato, Y.; Ellis, C. T.; Tischler, J. G.; Woods, C. R.; Giles, A. J.*, et al.* Sub-Diffractional Volume-Confined Polaritons in the Natural Hyperbolic Material Hexagonal Boron Nitride. *Nat. Commun.* **2014,** 5, 5221.

28. Malitson, I. H. Interspecimen Comparison of Refractive Index of Fused Silica. *J. Op.t Soc. Am.* **1965,** 55, 1205-1209.

29. Kischkat, J.; Peters, S.; Gruska, B.; Semtsiv, M.; Chashnikova, M.; Klinkmuller, M.; Fedosenko, O.; Machulik, S.; Aleksandrova, A.; Monastyrskyi, G.*, et al.* Mid-Infrared Optical Properties of Thin Films of Aluminum Oxide, Titanium Dioxide, Silicon Dioxide, Aluminum Nitride, and Silicon Nitride. *Appl. Optics.* **2012,** 51, 6789-6798.

30. Li, H. H. Refractive-Index of Silicon and Germanium and Its Wavelength and Temperature Derivatives. *J. Phys. Chem. Ref. Data* **1980,** 9, 561-658.

31. Green, M. A.; Keevers, M. J. Optical-Properties of Intrinsic Silicon at 300 K. *Prog. Photovoltaics* **1995,** 3, 189-192.

32. Nair, R. R.; Blake, P.; Grigorenko, A. N.; Novoselov, K. S.; Booth, T. J.; Stauber, T.; Peres, N. M. R.; Geim, A. K. Fine Structure Constant Defines Visual Transparency of Graphene. *Science* **2008,** 320, 1308-1308.

33. Yu, R. W.; Pruneri, V.; de Abajo, F. J. G. Resonant Visible Light Modulation with Graphene. *ACS Photonics.* **2015,** 2, 550-558.

34. Kim, T. Y.; Park, C. H.; Marzari, N. The Electronic Thermal Conductivity of Graphene. *Nano Lett.* **2016,** 16, 2439-2443.

35. Fong, K. C.; Schwab, K. C. Ultrasensitive and Wide-Bandwidth Thermal Measurements of Graphene at Low Temperatures. *Phys. Rev. X.* **2012,** 2, 031006.

36. Pop, E.; Varshney, V.; Roy, A. K. Thermal Properties of Graphene: Fundamentals and Applications. *MRS Bull.* **2012,** 37, 1273-1281.

37. Model Sr830 Dsp Lock-in Amplifier. https://www.thinksrs.com/downloads/pdfs/manuals/SR830m.pdf.

38. Collins, R. L.; Cosgrove, J. G. Temperature-Dependence of Johnson Noise. *Phys. Lett. A* **1974,** 48, 85-86.

39. Steinbach, A. H.; Martinis, J. M.; Devoret, M. H. Observation of Hot-Electron Shot Noise in a Metallic Resistor. *Phys. Rev. Lett.* **1996,** 76, 3806-3809.

40. McKitterick, C. B.; Prober, D. E.; Rooks, M. J. Electron-Phonon Cooling in Large Monolayer Graphene Devices. *Phys. Rev. B* **2016,** 93, 075410.

41. McKitterick, C. B.; Prober, D. E.; Karasik, B. S. Performance of Graphene Thermal Photon Detectors. *J. Appl. Phys.* **2013,** 113, 044512.

42. Xia, F. N.; Mueller, T.; Lin, Y. M.; Avouris, P. Ultrafast Graphene Photodetector. *Nat. Nanotechnol.* **2009**, 4, 839-843.

43. Wu, E. P.; Wu, D.; Jia, C.; Wang, Y. G.; Yuan, H. Y.; Zeng, L. H.; Xu, T. T.; Shi, Z. F.; Tian, Y. T.; Li, X. J. In Situ Fabrication of 2d WS2/Si Type-Ii Heterojunction for Self-Powered Broadband Photodetector with Response up to Mid-Infrared. *ACS Photonics* **2019,** 6, 565-572.

44. Wu, D.; Guo, J. W.; Du, J.; Xia, C. X.; Zeng, L. H.; Tian, Y. Z.; Shi, Z. F.; Tian, Y. T.; Li, X. J.; Tsang, Y. H.*, et al.* Highly Polarization-Sensitive, Broadband, Self-Powered Photodetector Based on Graphene/Pdse2/Germanium Heterojunction. *ACS Nano* **2019,** 13, 9907-9917.

45. Kruse, P. W. *Uncooled Thermal Imaging: Arrays, Systems, and Applications*; SPIE Optical Engineering Press: Bellingham, **2001**.

46. Xie, C. Z.; Aziz, M.; Pusino, V.; Khalid, A.; Steer, M.; Thayne, I. G.; Sorel, M.; Cumming, D. R. S. Single-Chip, Mid-Infrared Array for Room Temperature Video Rate Imaging. *Optica* **2017,** 4, 1498-1502.